

AIRCREW EXPOSURE FROM COSMIC RADIATION ON COMMERCIAL AIRLINE ROUTES

B. J. Lewis[†], M. J. McCall[†], A. R. Green[†], L. G. I. Bennett[†], M. Pierre[†],
U. J. Schrewe[‡], K. O'Brien[§] and E. Felsberger^{||}

[†]Royal Military College of Canada, P.O. Box 17000
Kingston Ontario, Canada K7K 7B4

[‡]Physikalisch Technische Bundesanstalt, Postfach 33 45
38023 Braunschweig, Germany

[§]Northern Arizona University, Flagstaff, Arizona 86011, USA

^{||}Technical University Graz, Petersgasse 16/4, 8010 Graz, Austria

Received June 27 2000, revised August 22 2000, accepted October 24 2000

Abstract — As a result of the recent recommendations of the ICRP 60, and in anticipation of possible regulation on occupational exposure of Canadian-based aircrew, an extensive study was carried out by the Royal Military College of Canada over a one-year period to measure the cosmic radiation at commercial jet altitudes. A tissue-equivalent proportional counter was used to measure the ambient total dose equivalent rate on 62 flight routes, resulting in over 20,000 data points at one-minute intervals at various altitudes and geomagnetic latitudes (i.e. which span the full cut-off rigidity of the Earth's magnetic field). These data were then compared to similar experimental work at the Physikalisch Technische Bundesanstalt, using a different suite of equipment, to measure separately the low and high linear energy transfer components of the mixed radiation field, and to predictions with the LUN transport code. All experimental and theoretical results were in excellent agreement. From these data, a semi-empirical model was developed to allow for the interpolation of the dose rate for any global position, altitude and date (i.e. heliocentric potential). Through integration of the dose rate function over a great circle flight path, a computer code was developed to provide an estimate of the total dose equivalent on any route worldwide at any period in the solar cycle.

INTRODUCTION

Jet aircrew are routinely exposed to levels of natural background radiation from galactic cosmic rays which are significantly higher than those present at ground level. In 1990, the International Commission on Radiological Protection (ICRP) recommended that aircrew be classified as occupationally exposed.⁽¹⁾ They also recommended a reduction in the occupational exposure (i.e. from 50 to 20 mSv.y⁻¹ averaged over 5 years, with not more than 50 mSv in a single year) as well as a reduction in the general population exposure (i.e. from 5 to 1 mSv.y⁻¹)⁽¹⁾. Recent studies of major Canadian airlines have determined that the exposure to most aircrew is comparable to that recorded in the Canadian National Dose Registry (Table 1)^(2,3). As a result, many countries around the world may have to develop regulatory policy in light of the ICRP recommendations requiring some form of exposure monitoring of aircrew. For example, the revised European Union (EU) Basic Safety Standard Directive, published in May 1996 (BSS96), requires that radiation protection measures for aircraft crew be incorporated into the national legislation of EU member states before 13 May 2000⁽⁴⁾. In the United

States, the Federal Aviation Administration (FAA) has formally recognised that aircrew members are occupationally exposed to radiation and should be subject to the same radiation protection policies practised by all other federal agencies⁽⁵⁾. Consequently, in 1994, the FAA published an advisory document to the commercial air carriers outlining an educational programme that should be implemented to inform crew-members of the nature of their radiation exposures and the associated health risks⁽⁶⁾. In Canada, an advisory circular by Transport Canada is being developed and will be issued shortly to recognise the occupational exposure of aircrew⁽⁷⁾.

Monitoring of the occupational exposure of aircrew could take several forms, such as with personal passive dosimetry (as in the nuclear industry) or by area monitoring with fixed instrumentation on board the aircraft. Alternatively, since the cosmic radiation exposure is relatively constant, a computer prediction program, based on either theory or on an experimental database, could be used to predict the aircrew exposure by using an estimate of the route dose and a knowledge of the flight frequency. If such a program proved successful, the cost and infrastructure of utilising such a tool would be considerably less than the other two options, i.e. the code predictions could be assured by a much reduced monitoring programme.

This paper describes the method of collecting and analysing radiation data by the Royal Military College

Contact author E-mail: lewis-b@rmc.ca

of Canada (RMC) from numerous worldwide flights using a tissue-equivalent proportional counter (TEPC) and other active and passive instrumentation which is able to characterise the complex cosmic radiation field⁽⁸⁾. The current measurements are further supported and successfully compared to other results that are derived from: (i) a similar measurement programme conducted at the Physikalisch Technische Bundesanstalt (PTB) with different instrumentation to measure separately the low and high linear energy transfer (LET) components of the mixed-radiation field at altitude^(9,10), and (ii) a theoretical treatment with a transport code⁽¹¹⁾. It is further shown how the RMC measurements can be encapsulated into a semi-empirical model/computer code to calculate the radiation dose for any flight in the world at any period in the solar cycle. Thus, this experimentally based code could find application for aircrew monitoring in light of possible regulatory requirements in various countries around the world.

RADIATION FIELD CHARACTERISTICS AT JET ALTITUDES

The radiation that is found at jet aircraft altitudes (~6.1 to 18 km) is produced from the interaction of primary galactic cosmic ray (GCR) particles with the Earth's atmosphere. The GCRs consist of ~90% protons, 9% alpha particles and 1% heavy nuclei typically ranging from carbon to iron⁽¹²⁾. Most of these particles have energies between 100 MeV and 10 GeV, which can extend up to 10²⁰ eV⁽¹²⁾. The sun is also a sporadic source of X rays and charged particles (i.e. mainly protons, some alpha particles and a few heavy nuclei) as a result of magnetic energy release in solar flares. These solar particle events (SPE) are much more frequent during the active phase of the solar cycle and can occur over hours to days with maximum particle energies of between 10 and 100 MeV, possibly reaching up to 10 GeV once in a decade⁽¹³⁾. Although the effect of GCRs to aircrew exposure is generally much greater than the occasional SPE, a rare solar event could lead to a significant dose at supersonic altitudes, e.g. it is estimated that an event on 23 February 1956 yielded a dose equivalent rate of ~10 mSv.h⁻¹ at 20 km⁽¹⁴⁾.

The charged GCRs will interact with the solar mag-

netic field that is carried by the outward-flowing solar wind due to the frozen-in condition from the high conductivity of the plasma, resulting in a deflection of these particles. A diffusion-convection model can be used to describe this solar modulation on the GCR spectrum, which is equivalent to that produced by a heliocentric potential, U⁽¹⁵⁾. The time dependence of the heliocentric potential with the solar cycle can be determined from particle flux measurements on balloons and spacecraft, as well as from ground-level measurements on Earth with neutron monitors^(16,17). For instance, the heliocentric potential as derived from monitoring is available monthly online⁽¹⁸⁾. When solar sunspot activity is at a maximum (approximately every eleven years), the increased solar field acts to screen out low-energy GCRs. Thus, cosmic ray intensities also vary in a cyclical pattern, but in a manner anticoincident with the solar activity (Figure 1).

The GCRs that are not deflected by the solar magnetic field now encounter the magnetic field of the Earth, which can provide an effective shield against lower energy particles. These charged particles are deflected by the Lorenz force in which their trajectories have a curvature of radius $r = R_p/B_p$ ⁽¹⁵⁾. Here B_p is the component of the Earth's magnetic field perpendicular to the direction of the motion and R_p is the so-called magnetic rigidity, which is related to the particle's momentum (p) and charge (q),

$$R_p = \frac{pc}{q} \tag{1}$$

where c is the speed of light⁽²¹⁾. The penetrating ability of these particles is dependent on their angle of incidence and rigidity. A particle can enter the Earth's atmosphere if its magnetic rigidity, R_p , is greater than the vertical cut-off rigidity of the Earth's magnetic field, R_c , at its point of entry. The vertical cut-off rigidity (in GV) has been derived by Shea *et al* and is related to the geomagnetic latitude, B_m , (in radians). In particular, as derived by Shea *et al* as a slight adaptation of the original Störmer equation⁽²²⁾,

$$R_c = 16.237L^{-2.0353} \tag{2a}$$

in which the McIlwain L-parameter is given by

$$L = \frac{r_e}{\cos^2 B_m} \tag{2b}$$

Table 1. Average annual occupational exposures in Canada*.

Category	Occupation	Annual exposure (mSv)
Nuclear power	Nuclear fuel handler	4.73
Industry and Research	Industrial radiographer	2.90
Uranium mining	Underground uranium miner	2.04
Medicine	Nuclear medicine technologist	1.44
Airline	Aircrew (pilots and flight attendants)	~1 to 5

*Based on information in References 2 and 3 (preliminary analysis of 1998 occupational exposure).

Here r_c is the distance from the Earth's dipole centre (in units of Earth radii) defined by

$$r_c = \left(\frac{1}{a} \right) \left\{ \frac{b}{\sqrt{(1 - \epsilon^2 \cos^2 B_m)}} + A \right\} \quad (2c)$$

where b ($= 6357$ km) is the minimum (polar) radius of the Earth, ϵ ($= 8.20 \times 10^{-2}$) is the eccentricity, a ($= 6372$ km) is the average radius of the Earth, and A (≈ 11 km) is the typical altitude of the aircraft. Equation 2 is a best-estimate composite expression for three epochs from 1955 to 1980. The geomagnetic latitude, B_m , in turn, can be calculated from the geographic latitude and longitude (λ, ϕ) according to⁽²³⁾:

$$\sin B_m = \sin \lambda \sin \lambda_p + \cos \lambda \cos \lambda_p \cos(\phi - \phi_p) \quad (3)$$

where $\lambda_p = 79.3^\circ\text{N}$ and $\phi_p = 289.89^\circ\text{E}$ (the position of the geomagnetic north pole). A higher value of the cut-off rigidity R_c indicates a reduced penetration at the given global position. The cut-off rigidity is highest at the equator where the magnetic field lines are parallel to the Earth's surface, which reflect vertically incident GCRs with a rigidity less than 16 GV. On the other hand, at the poles, there is a maximum penetration where the field lines are almost vertical with a zero cut-off rigidity. At jet aircraft altitudes during a minimum in the solar cycle (i.e. when the corresponding galactic radiation is at a maximum), the galactic radiation is 2.5 to 5 times more intense at the poles than at the equatorial regions⁽²⁴⁾. The cut-off rigidity curve displays another interesting feature, the so called 'geomagnetic knee', which is a fairly large region above approximately 50°N in Canada or 70°N in Siberia where the radiation levels are constant with increasing latitude.

The GCRs are subject to further shielding by the

Earth's atmosphere, where these particles interact with atmospheric nitrogen and oxygen nuclei. In each collision, a proton loses on average $\sim 50\%$ of its energy, which results in a production of secondary particles like protons, neutrons, and π and K mesons⁽¹⁵⁾. The target nuclei can also produce protons, neutrons and alpha particles by evaporation. Particles generated by successive interactions with the primary and/or secondary particles therefore produce a cascade of hadrons in the atmosphere. These secondary particles also decay radioactively. The charged mesons form muons which are able to reach the Earth's surface where they provide the greatest contribution to the ground cosmic exposure. The muons can also decay by the weak interaction into electrons, while the neutral pions may decay into photons which, by pair production, can further result in a formation of electrons and positrons^(15,25). The build-up of these secondary particles competes with their reduction through energy loss and further interactions with other atmospheric nuclei. This competition results in dose rates which vary with altitude, reaching a maximum level at about 20 km above sea level, known as the Pfozter maximum. Calculations of the propagation of atmospheric cosmic rays can be evaluated with the LUN transport code which is based on an analytic solution of the Boltzmann transport equation⁽²⁶⁾. This code has now been extended to account for the hadron cascade with energies down to 10 MeV/nucleon, and employs a neutron spectrum down to thermal energies (as derived from a FLUKA code analysis). In addition, Monte Carlo methods are typically employed for the different radiation components at lower energies, although the FLUKA code can account for particle energies up to 10 TeV^(27,28). The relative abundance of different par-

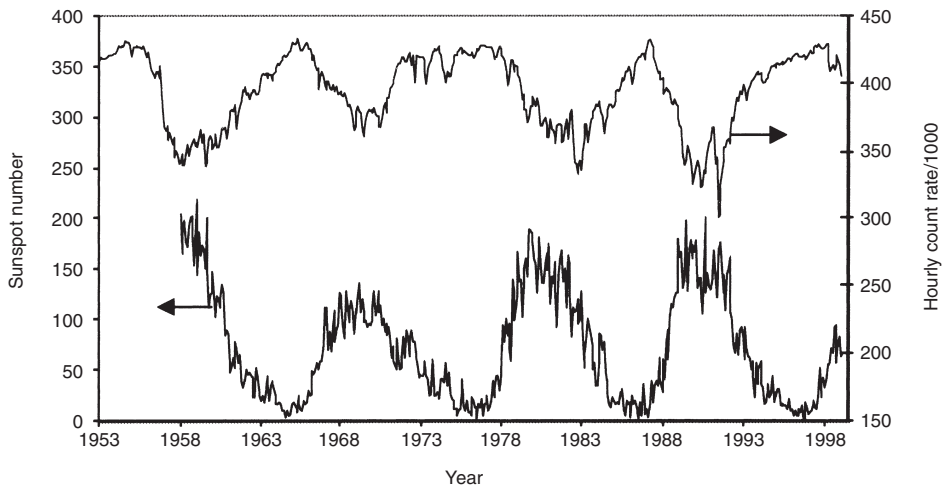


Figure 1. Plot of neutron count rate and sunspot number plotted against date^(19,20). Sunspot number per month (which is an indication of the heliocentric potential); monthly average of the hourly neutron count from the Climax, Colorado ground-based neutron monitor.

icles is calculated in Figure 2(a) with no geomagnetic shielding during a solar minimum. This calculation shows the particle fluence rate as a function of atmospheric depth as obtained with a FLUKA analysis and the environmental model of Badhwar^(15,29). These calculations are also compared with those derived from LUIIN at the pole during solar minimum conditions. The FLUKA and LUIIN calculations are in reasonable agreement except for the proton contribution where FLUKA predicts a greater particle fluence rate by a factor of 2.

As previously mentioned, the secondary particles are seen to reach a maximum in Figure 2(a) and then decrease with absorption while, in the upper part of the atmosphere, the protons (which are mainly primary particles) show a continuously decreasing fluence rate. Although there is no maximum for the primary protons at high latitudes, this feature becomes more prominent at low latitudes where the high cut-off rigidity of the Earth's magnetic field removes a significant fraction of the low energy primaries as predicted by LUIIN in Figure 2(b).

EXPERIMENTAL PROCEDURE

Since radiation effects vary with altitude, geomagnetic latitude and heliocentric potential, the primary goal of this research was to obtain data covering these parameters that were valid for the complex spectrum at aircraft altitudes.

The only single instrument for a complete measurement of the cosmic mixed-radiation field is a tissue-equivalent proportional counter (TEPC). It provides not only an indication of the total dose equivalent (with a

simulation of a tissue-equivalent site with a diameter of 2 μm), but also the microdosimetric distribution of the radiation as a function of the lineal energy. The lineal energy can be used as a surrogate measurement of the linear energy transfer (LET) for the cosmic radiation spectrum⁽²⁾. The TEPC used in this study had a 5" diameter detector built by Far West Technology, and was designed by Battelle Pacific Northwest National Laboratories to be an extremely portable instrument (Figure 3). This instrument fits into any overhead bin and is powered by batteries which last up to five days of operation. It is simple to operate (off/on switch only) and stores a microdosimetric spectrum every minute for up to thirty days of operation.

The TEPC was calibrated initially by the manufacturer using ¹³⁷Cs and ²⁵²Cf sources. This calibration was checked routinely with an internal ²⁴⁴Cm source, which, in normal operation, is shielded from the detector cavity by a magnetic shutter. Since the radiation field at jet altitudes is so complex, the response of the TEPC was verified in several types of terrestrial radiation fields prior to use at jet altitudes. For the majority of the in-flight measurements, aircrew turned on the TEPC prior to takeoff and off after landing, and provided positional data consisting of the flight course and altitude history. Since the TEPC has its own internal clock, the TEPC measurements could then be correlated to the aircraft position (geomagnetic latitude and altitude) at one-minute intervals. The stored data were downloaded at the laboratory to provide an output of absorbed dose rate, D, and dose equivalent rate, H. In addition to these outputs, the raw spectral TEPC data could also be output as a microdosimetric dose

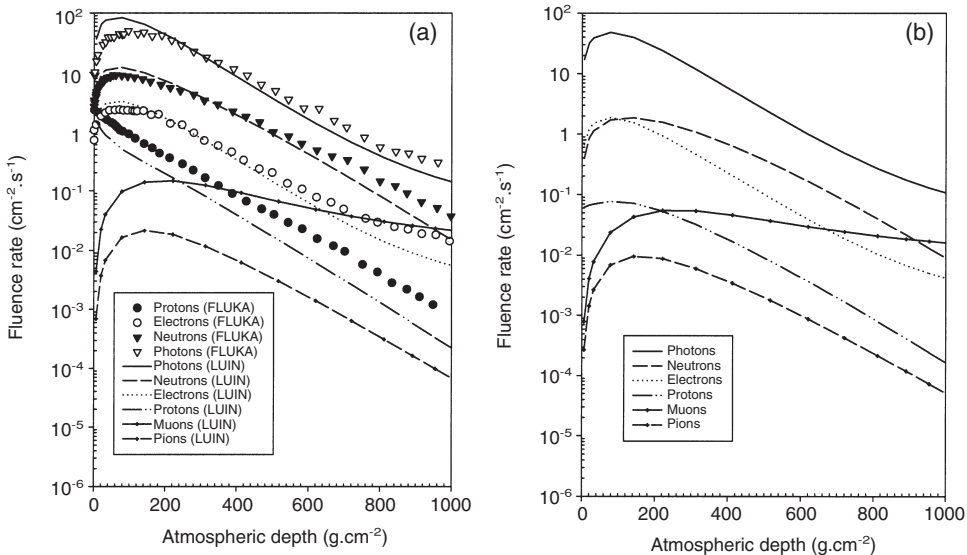


Figure 2. Integrated fluence rate plotted against atmospheric depth for different particles. (a) Comparison of the fluence rate as calculated by FLUKA and LUIIN during solar minimum with no geomagnetic shielding. (The FLUKA calculations are taken from Reference 15.) (b) The fluence rate as calculated by LUIIN during solar minimum at the equator.

distribution to provide an estimate of the average quality factor, \bar{Q} , of the radiation field⁽³⁰⁻³²⁾.

In addition to the portable TEPC, different types of passive and active detectors were also used on several scientific flights to measure the individual low-LET (ionising) and high-LET (neutron) components of the mixed-radiation field in the RMC study (which can be appropriately summed for comparison to the TEPC results). The various portable instruments used in this study included: (i) temperature-compensated neutron bubble detectors (BD-PND) from Bubble Technology Industries (BTI); (ii) a battery-powered Eberline FHT 191 N ionisation chamber (IC); (iii) aluminium oxide (Al₂O₃) thermoluminescent detectors (TLDs); (iv) a Siemens Electronic Personal Dosimeter (EPD); and (v) a passive dosimeter box assembled by the National Radiological Protection Board (NRPB) in the United Kingdom, which contained 30 TLDs and 24 polyallyldiglycol carbonate (PADC) etched track detectors.

GROUND-BASED MEASUREMENTS

In support of the in-flight study, the operation of the TEPC was verified and calibrated using several common radioisotopic sources, such as ¹³⁷Cs, ²⁵²Cf, ²⁴¹Am-⁹Be and ²³⁹Pu-⁹Be⁽³⁰⁾. As detailed in Appendix 1, the TEPC response was also evaluated with a monoenergetic neutron source from 0.144 to 14.8 MeV at the PTB, along with neutron bubble detectors that had been

employed extensively in earlier studies to measure the neutron component of the cosmic field.

The individual microdosimetric spectra recorded by the TEPC in these various fields represent the different constituents present in the radiation field at high altitudes (i.e. the gamma and neutron components of the field). The energy spectrum of the high LET (i.e. neutron) component of the radiation field created by cosmic rays at jet altitudes can be simulated on the ground by the radiation field produced behind concrete shielding at accelerator facilities (Figure 4). The CERN/European Commission high energy reference field facility (CERF) has been used for this purpose since 1993⁽⁴⁶⁾. This facility is set up at one of the secondary beams from the Super Proton Synchrotron at CERN. The particles (protons and pions) from a charged hadron beam hit a copper target, 50 cm thick and 7 cm in diameter. The secondary particles resulting from this interaction are then filtered by an 80 cm thick concrete shielding placed above the copper target. As a further measurement, the microdosimetric spectrum recorded by the TEPC on top of this shielding is compared to an in-flight one in Figure 5. Although the shape of the high LET (>10 keV.μm⁻¹) portion is similar in both spectra (as expected from the similarities in the neutron spectra), the relative area represented by the high LET portion of each spectrum is significantly different. This feature is a direct result of the difference in the relative proportion of neutrons in each field where the neutron

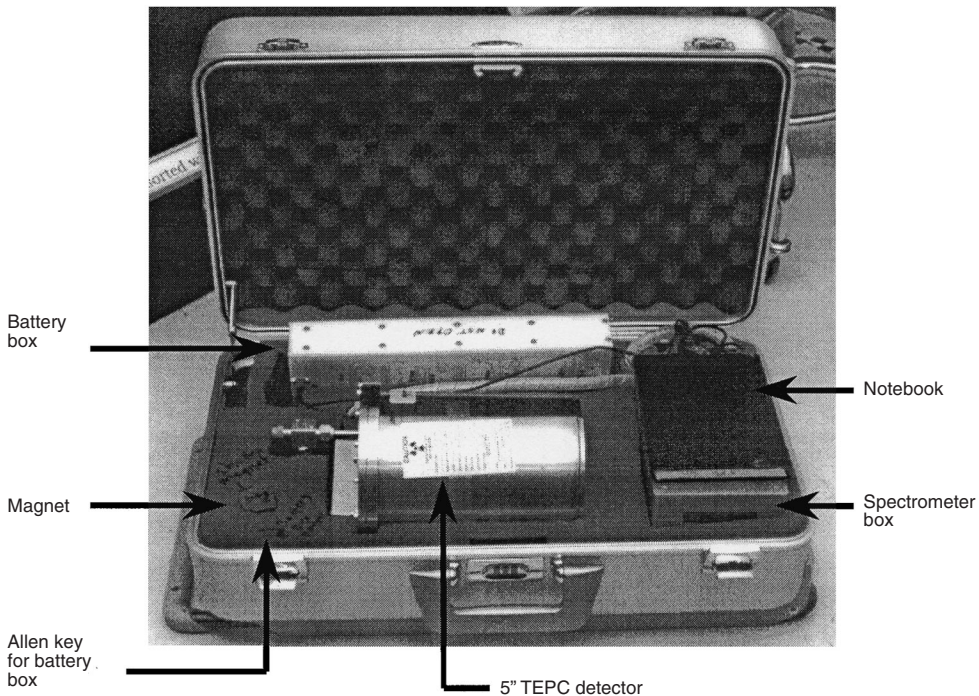


Figure 3. Arrangement of TEPC components in the carry-on case.

field in CERF contributes about 85% of the total dose equivalent, compared to approximately 50% at jet altitudes. As a result, the relative area under the curve for $y > 10 \text{ keV}\cdot\mu\text{m}^{-1}$ is much greater in the CERF spectrum (Figure 5(a)) than in the jet-altitude spectrum (Figure 5(b)). In addition, the low LET portion of the spectrum obtained at CERF is dominated by a background muon contribution which is not present at jet altitudes.

The microdosimetric quantities of the frequency-mean lineal energy, \bar{y}_F , the dose-mean lineal energy, \bar{y}_D , and the average quality factor, \bar{Q} , are defined in the Appendix of Reference 2. Values of these quantities for the various terrestrial sources and the CERF spectrum are given in Table 2. The quantity \bar{y}_F gives the average lineal energy per event, but the quantities \bar{y}_D and \bar{Q} are more useful in radiation protection since they are more

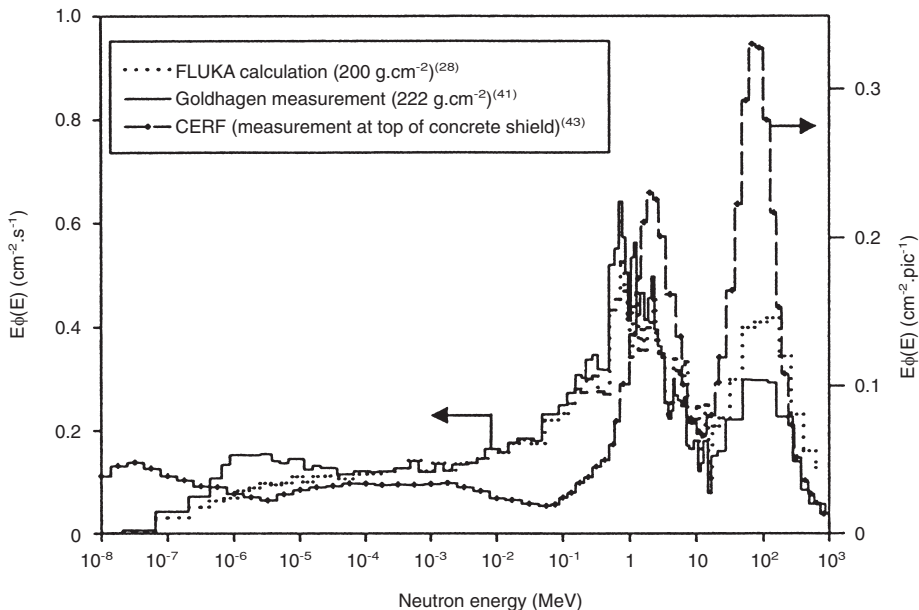


Figure 4. Comparison of measured, calculated and simulated cosmic ray neutron spectra (see text in Appendix 1).

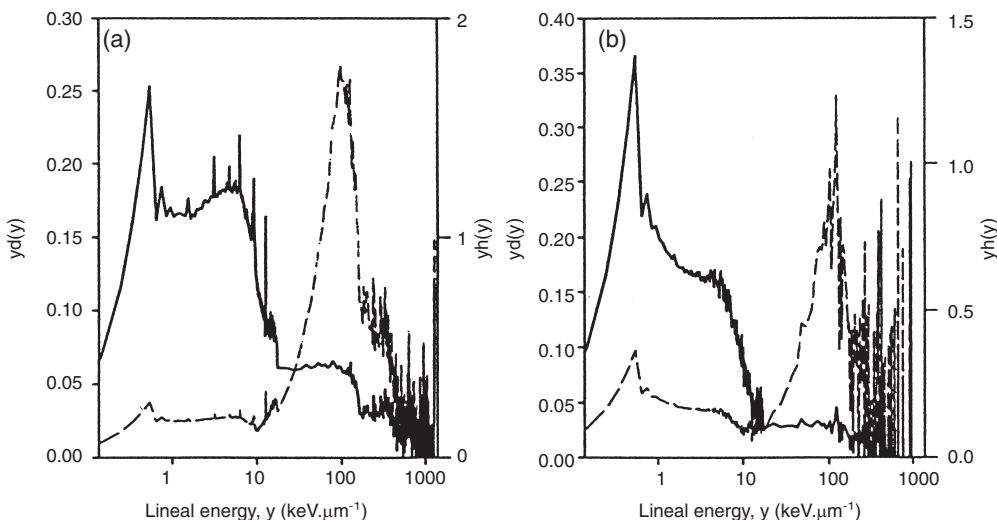


Figure 5. Comparison of microdosimetric absorbed dose and dose equivalent distributions obtained: (a) on top of the concrete shielding at CERF at a field intensity of 3500 Precision Ion Chamber (PIC) counts per pulse (summed over 3 h), and (b) on a 7 h flight between Toronto and Zurich at an altitude of 11.1 km. (—) $y\phi(y)$, (---) $yh(y)$.

representative of the relative biological effectiveness (RBE) of the measured radiation. In particular, \bar{Q} should provide an approximation of the ICRP 60 radiation weighting factor, w_R , as derived from a ratio of the dose equivalent (H) to the absorbed dose (D) in the TEPC analysis. For instance, the experimental \bar{Q} value of 1.1 obtained for gamma rays from a ^{137}Cs source agrees quite well with a w_R value of 1 as recommended by ICRP 60. As expected, fields with more biologically-damaging particles (such as the ^{239}Pu - ^9Be neutron field) will have higher values of \bar{Q} and \bar{y}_D . The values of these quantities obtained from terrestrial sources can provide a useful comparison to the values obtained from the radiation field at jet altitudes.

AT-ALTITUDE MEASUREMENTS

The TEPC was used as the primary instrument to take dosimetric measurements and microdosimetric spectra on board 62 worldwide flights flown at altitudes between 4.5 and 12.4 km from September 1998 to October 1999. A typical dose distribution for a trans-Atlantic flight is shown in Figure 5(b). For a portion of these flights at altitudes greater than 8.5 km, values of

\bar{y}_F , \bar{y}_D and \bar{Q} were obtained from TEPC spectral data summed over an entire flight (Table 3). The values of all three of these quantities are all very similar to those obtained from the radiation field on top of the shielding at CERF in Table 2. On all flights, the \bar{Q} values are greater than 1 and the \bar{y}_D values are greater than 10 $\text{keV}\cdot\mu\text{m}^{-1}$, which indicates a significant high LET ($> 10 \text{ keV}\cdot\mu\text{m}^{-1}$) contribution to the radiation field. Thus, as shown in Figure 6, the aircraft environment is dominated by radiation with a higher Q value, for which there is a greater uncertainty in the biological risk coefficient⁽⁴⁷⁾. In contrast, most terrestrial occupational exposures are dominated by radiation with a lower deposition energy, for which $Q \sim 1$, and the risk coefficients are better known.

In addition to the TEPC, radiation levels were also monitored with various pieces of instrumentation that are sensitive to different components of the mixed radiation field on several representative flight routes (see Table 4). The dose equivalent arising from the neutron (i.e. high LET) component of this field was measured using BDs or the PADC detectors of the NRPB box. In addition, on some flights, the dose equivalent arising from the non-neutron (i.e. mainly low LET) component was

Table 2. Microdosimetric quantities obtained from ground-based sources.

Source	Type of radiation	\bar{y}_F ($\text{keV}\cdot\mu\text{m}^{-1}$)*	\bar{y}_D ($\text{keV}\cdot\mu\text{m}^{-1}$)	\bar{Q}
^{137}Cs	γ rays	0.36 ± 0.13	7.2 ± 0.8	1.1 ± 0.2
CERF	neutrons, muons, γ rays	0.50	30 ± 3	3.8 ± 0.7
^{239}Pu - ^9Be	neutrons, γ rays	1.39	51 ± 6	9 ± 2
^{244}Cm	α particles	14.0	150 ± 20	24 ± 4

*The maximum error on \bar{y}_F is 35%, most of which is associated with the extrapolation to zero lineal energy; thus, this error will be most significant for gamma ray spectra.

Table 3. Microdosimetric quantities measured on Canadian-based flights.

Global flight region	Routes covered*	\bar{y}_F ($\text{keV}\cdot\mu\text{m}^{-1}$)	\bar{y}_D ($\text{keV}\cdot\mu\text{m}^{-1}$)	\bar{Q}
Trans-Atlantic	YYZ-LHR (return)	0.358	14 ± 2	2.3 ± 0.4
	YYZ-FRA (return)			
	YYZ-ZRH (return)			
Trans-Canada	YUL-LHR	0.359	15 ± 2	2.3 ± 0.4
	LHR-YVR			
	YYZ-YVR (2)			
Caribbean	YVR-YYZ (3)	0.340	13 ± 2	2.2 ± 0.4
	YYZ-BGI			
Trans-Pacific	BGI-YYZ	0.334	15 ± 2	2.2 ± 0.4
	YVR-KIX			
	KIX-YVR			

*Airport codes are: YYZ-Toronto International; LHR-Heathrow, London, UK; FRA-Frankfurt, Germany; ZRH-Zurich, Switzerland; YUL-Dorval, Montreal; YVR-Vancouver; BGI-Bridgetown, Barbados; KIX-Osaka, Japan.

measured independently using either an IC, TLDs or an EPD. Both the TLDs and NRPB box correspond to integrated values over several flight legs. Table 4 also shows different methods for estimating the total dose equivalent with various combinations of instrumentation. The measured BD/TEPC ratio for the dose equivalents in Table 4 can also be used to convert the extensive BD data measured in an earlier study (Reference 2) to a total dose equivalent (for all particle types). Considering an average of the flights in the given global flight regions of Table 4, this ratio (i.e. neutron fraction) ranges from 0.42 to 0.45, except for the equatorial region where a lower value of 0.33 is observed due to geomagnetic shielding effects (as also revealed in transport calculations).

An estimate of the low LET dose equivalent can also be obtained from the TEPC by including only those data points at lineal energies less than $10 \text{ keV} \cdot \mu\text{m}^{-1}$. The TEPC gamma measurements in Table 4 are always ~10–15% lower than that measured by the IC. This systematic discrepancy suggests that the IC is responding to ionising particles with higher lineal energy values as well. The EPD readings are also consistently lower than the IC measurements by at least 20%. This result suggests that the EPD (as normally used in the nuclear industry for ionising dose assessment) cannot be directly used for aircrew exposure assessment unless the EPD measurements are suitably scaled to an instrument with an improved response for the more penetrating ionising particles of higher energy and charge. The low LET dose equivalent (from the IC or TLDs) can be summed to the high LET (neutron) value to obtain an estimate

of the total dose equivalent. The data in Table 4 show that this procedure results in a value which is ~90% of that measured by the TEPC. This slight discrepancy can be related to the fact that the IC and TLDs are referenced to a photon-equivalent field (i.e. with a mean quality factor $\bar{Q} = 1$), and therefore do not take into account an enhanced quality factor for those ionising particles actually present in the cosmic spectrum with lineal energies greater than $10 \text{ keV} \cdot \mu\text{m}^{-1}$ (such as protons). As mentioned above, the data indicate that the IC is indeed detecting such particles. In fact, ~18% of the absorbed dose from the non-neutron component can be attributed to protons, although this fraction is somewhat dependent on altitude and latitude^(48,49). A mean quality factor of 1.5 has been proposed to account for the enhanced proton contribution such that⁽⁴⁸⁾:

$$H_{\text{IC,TLD}} = \{[1 \times (1 - 0.18)] + [1.5 \times 0.18]\}D_{\text{IC,TLD}} \approx 1.1D_{\text{IC,TLD}} \quad (4)$$

where H is the corrected ambient dose equivalent for the non-neutron component and D is the absorbed dose as measured with either the IC or TLDs. Thus, the IC and TLD measurements should be multiplied by a correction factor of 1.1 in order to account for the dose equivalent effect from protons. This proton component is already appropriately weighted with the use of the Q(LET) relationship for the TEPC⁽²⁾. If the IC and TLD measurements are multiplied by this correction factor, the BD and IC measurements will sum to be about 95% of the TEPC one, which is well within the measurement uncertainty. However, even this small discrepancy can be somewhat attributed to the under-response of the BDs to neutrons of very high energy where the microscopic cross sections of the superheated detector liquid are known to decrease with increasing energy (see Figure A1.2 in Appendix 1).

In conclusion, the summed results from the various independent equipments are self-consistent with the TEPC results, providing further confidence in the use of the TEPC data for model development presented in the next section.

MODEL DEVELOPMENT (FOR ROUTE-DOSE PREDICTION)

The raw TEPC output from the flights (corresponding to about 20,000 lineal energy spectra) can also be processed to provide a dose equivalent rate (every minute). However, it was decided that the spectral data be summed over five-minute intervals and the data smoothed using a least squares method developed by Savitzky and Golay⁽⁵⁰⁾ to reduce the relative error in the data to approximately 18%. This method of data treatment was applied to the TEPC spectral data obtained from 36 flights (i.e. a sub-set of the original 62 flights that was used specifically for model development). This analysis resulted in the dose equivalent rate data plotted as a function of altitude and geomagnetic latitude as

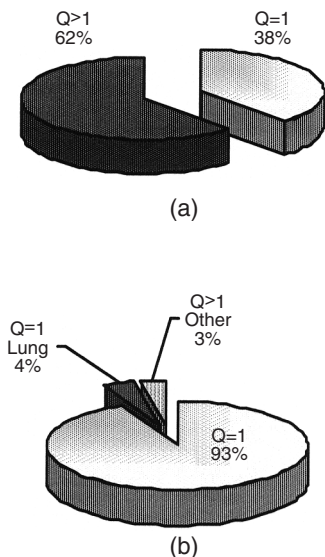


Figure 6. Quality factor of radiation exposures for: (a) aircrew on board a trans-Atlantic flight at 11.2 km (based on the data in Figure 5(b)), and (b) US atomic radiation workers (based on NCRP Report 93)⁽⁴⁷⁾.

AIRCREW EXPOSURE FROM COSMIC RADIATION

shown in Figure 7. This figure shows a consistent symmetry between altitude curves, which is due to the shielding effect of the atmosphere. The altitude A (in km) can also be related to an atmospheric depth h (in g.cm⁻²) (or atmospheric pressure p (in mbar)) in accordance with the relation⁽⁵¹⁾:

$$h = \frac{p}{0.98} = \begin{cases} 1.02p_0(1 - 0.0227A)^{5.26}, & A \leq 10.9 \\ 0.2276p_0 \exp[-0.1587(A - 10.94)], & A > 10.9 \end{cases} \quad (5)$$

where p₀ = 1013.25 mbar. In fact, if the dose equivalent

Table 4. Summary of results from fully instrumented flights.

Flight route	Date	Total flight time (min)	Neutron dose equivalent (μSv)		Non-neutron dose equivalent** (μSv)					Total dose equivalent (μSv)		
			BD*	NRPB PADC	TEPC Gamma	IC	TLD	EPD (H _p)	NRPB TLD	TEPC	BD + (IC or TLD)	NRPB box
A. Domestic flights												
YYZ-YVR	Feb 99	310	11 ± 1		11 ± 1						30 ± 5	
YVR-YYZ	Feb 99	229	15 ± 2		10 ± 1						29 ± 4	
YVR-YYZ	Mar 99	235	9 ± 1		8 ± 1						19 ± 3	
YTR-YWG	Oct 99	128	5 ± 2		4.8 ± 0.5	5.6 ± 0.6		5			12 ± 2	11 ± 2
YOW-YVO	Jul 99	43	0.3 ± 0.3		0.22 ± 0.02	0.26 ± 0.03	-	-			0.8 ± 0.1	0.6 ± 0.3
YVO-YFB		140	5.4 ± 0.9		3.7 ± 0.4	4.4 ± 0.4	-	-			10 ± 2	10 ± 1
YFB-YSR		97	1.6 ± 0.9		1.6 ± 0.2	1.8 ± 0.2	-	-			4.7 ± 0.7	3.4 ± 0.9
YSR-YFB		99	3.1 ± 0.9		1.9 ± 0.2	2.1 ± 0.2	-	-			5.1 ± 0.8	5.2 ± 0.9
YFB-YOW		153	6 ± 2		5.0 ± 0.5	5.7 ± 0.6	-	-			14 ± 2	12 ± 2
Total trip		532	16 ± 5		12 ± 1	14 ± 1	9 ± 5	9			35 ± 6	31 ± 5
B. Trans-Atlantic flights												
YYZ-LHR	Oct 98	395	13 ± 2	-	12 ± 1			-			33 ± 5	-
LHR-YYZ		453	15 ± 2	-	13 ± 2			-			37 ± 6	-
Round trip		848	28 ± 4	28 ± 13	25 ± 3			26 ± 2		28 ± 2	70 ± 11	54 ± 4
YYZ-FRA	Feb 99	414	16 ± 2		17 ± 2						43 ± 6	
FRA-YYZ	Feb 99	544	19 ± 4		21 ± 2						50 ± 8	
YUL-LHR	Mar 99	380	15 ± 2		15 ± 2						37 ± 6	
LHR-YVR	Mar 99	560	22 ± 2		23 ± 3						57 ± 8	
YYZ-ZRH	Jun 99	436	19 ± 2		17 ± 2	20 ± 2					45 ± 6	39 ± 3
ZRH-YYZ	Jun 99	487	20 ± 3		19 ± 2	23 ± 2					50 ± 7	43 ± 4
YTR-RMI	Oct 99	449	22 ± 2	~24	17 ± 2	19 ± 2		14	~13		43 ± 6	41 ± 3
RMI-EINN	Oct 99	154	-		4.0 ± 0.4	4.6 ± 0.5		-	-		10 ± 2	-
EINN-YOW		382	-		13 ± 1	15 ± 1.5		-	-		33 ± 5	-
YOW-YTR		35	-		0.07 ± 0.01	0.10 ± 0.01		-	-		0.35 ± 0.05	-
Total trip		571	21 ± 2	~24	17 ± 2	20 ± 2		16	~13		43 ± 7	41 ± 3
C. Trans-Pacific flights												
YVR-KIX	Mar 99	611	20 ± 4		20 ± 2						50 ± 7	
KIX-YVR	Mar 99	512	18 ± 2		16 ± 2						35 ± 5	
YVR-HNL	Oct 99	340	6 ± 1		7.5 ± 0.8	8.8 ± 0.9		6			16 ± 2	15 ± 1
HNL-YWG	Oct 99	393	11 ± 2		12 ± 1			9			~28 ± 4	
D. Caribbean flights												
YYZ-BGI	Apr 99	270	7 ± 2		7 ± 1			-			17 ± 3	-
BGI-YYZ		330	11 ± 2		10 ± 1			-			23 ± 4	-
Round trip		600	18 ± 4		17 ± 2			21 ± 2			40 ± 7	39 ± 4
E. Equatorial region												
HNL-NZAA	Oct 99	512	7 ± 2		10 ± 1	11 ± 1		8			21 ± 3	18 ± 2
NZAA-HNL	Oct 99	476	6 ± 1		9.4 ± 0.9			8			18 ± 3	

*The error quoted on the bubble detector readings represents the standard deviation (σ) on the reading of six different detectors.

**Based on a mean quality factor of 1.

rate data are plotted in a semi-logarithmic fashion against the atmospheric depth, h , a linear relationship is expected (as suggested from Figure 2 for the given range of atmospheric depth). The slope of the resulting line corresponds to an effective relaxation length for the given particles in the atmosphere, ξ_s . This result is indeed depicted in Figure 8, where the original data are plotted for different geomagnetic positions of 0, -30, 30, 45, 60, 75 and 90 degrees. An average slope of the resulting lines yields a value of $\xi_s = 0.0062 \text{ cm}^2.\text{g}^{-1}$, which is in excellent agreement with other literature values^(52,53).

This relaxation length (valid over the altitudes 9.4 to 11.8 km) can be used to normalise the data in Figure 7 to a specific altitude. In particular, the dose rate at 10.6

km (i.e. $h_o = 243 \text{ g.cm}^{-2}$) can be derived from the dose rate at any atmospheric depth according to the scaling function:

$$\frac{\dot{H}(h)}{\dot{H}_o} = \exp [-\xi_s (h - h_o)] \quad (6)$$

Normalising all data from various altitudes to 10.6 km in this manner yields Figure 9.

Unfortunately, Equation 6 cannot be extrapolated to altitudes near or above ~20 km because of the effect of secondary particle build-up (see Figure 2). However, a more general function can be derived to account for such effects. The incident cosmic radiation (i.e. protons) will be absorbed in the upper layer of the atmosphere. Thus, the rate of change of the primary particle intensity I_p (particle. $\text{m}^{-2}.\text{s}^{-1}$) with respect to a penetration distance z can be described by a simple (first-order) absorption law:

$$\frac{dI_p}{dz} = -k\rho I_p \quad (7)$$

where k (in $\text{m}^2.\text{kg}^{-1}$) is an absorption coefficient and ρ (in kg.m^{-3}) is the density of the atmosphere. The atmospheric density decreases exponentially with altitude, or in terms of the penetration distance z ⁽²³⁾:

$$\rho(z) = \rho_o e^{z/H} \quad (8)$$

where ρ_o is the value of ρ at some arbitrary level at which z is taken to be zero. Here the quantity H is the so called 'scale height' as given by⁽²³⁾:

$$H = \frac{kT}{mg} \quad (9)$$

where k is Boltzmann's constant ($= 1.38 \times 10^{-23} \text{ J.K}^{-1}$), T is the kinetic temperature (in K), m is the molecular weight of air ($= 29.0 \text{ u} \times 1.66 \times 10^{-27} \text{ kg.u}^{-1} = 4.81 \times 10^{-26} \text{ kg}$) and g is the acceleration due to gravity ($= 9.80 \text{ m.s}^{-2}$)⁽⁵⁴⁾. Assuming a typical atmospheric temperature of ~220 K⁽⁵⁴⁾, H is evaluated as 6.4 km. Since

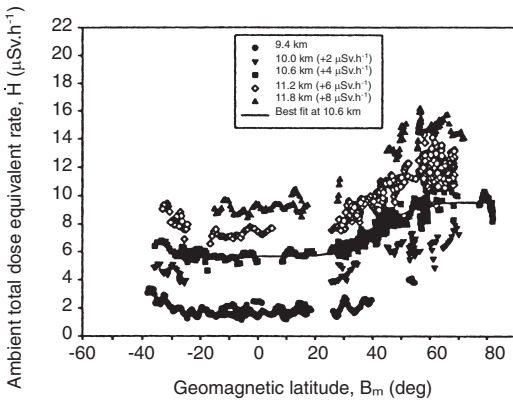


Figure 7. Experimental dose rate data plotted against geomagnetic latitude for various altitudes. (The curves are displaced for improved clarity by the values given in the figure.)

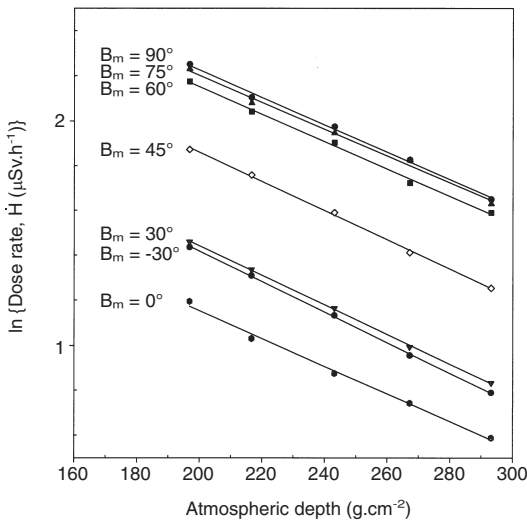


Figure 8. Plot of $\ln(H)$ against atmospheric depth at various global positions.

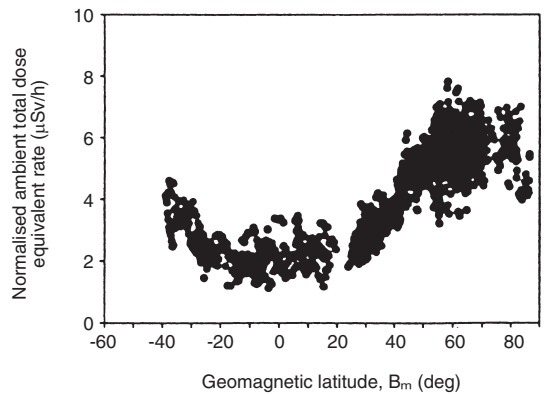


Figure 9. Dose rate (normalised to 10.6 km) relative to geomagnetic latitude.

h and ρ are both functions which decrease exponentially with altitude, it is not surprising that there is roughly a linear relationship among them, i.e. $h = \kappa\rho$, where κ corresponds to a slope of 7.1 km⁽⁵⁴⁾.

Thus, using the chain rule $\frac{dI_p}{dz} = \frac{dI_p}{dh} \cdot \frac{dh}{d\rho} \cdot \frac{d\rho}{dz}$, and calculating the derivative $d\rho/dz$ from Equation 8, with $dh/d\rho = \kappa$, Equation 7 yields:

$$\frac{dI_p}{dh} = -k_o I_p \quad (10)$$

where $k_o = kH/\kappa$. Equation 10 can therefore be directly integrated,

$$I_p(h) = I_{po} e^{-k_o h} \quad (11)$$

where I_{po} is the intensity at the top of the atmosphere at $h = 0$. Analogous to Chapman layer theory in the formation of the ionosphere, the production of secondary particles can be assumed to be proportional to the rate of absorption of the primary particles, dI_p/dz , with an effective proportionality constant β ⁽²³⁾. Thus, accounting for this source, and a first-order loss due to absorption in the atmosphere with a coefficient μ , the conservation statement for the intensity, I_s , of the secondary particles is:

$$\frac{dI_s}{dz} = \beta k_p I_p - \mu I_s \quad (12a)$$

or equivalently

$$\frac{dI_s}{dh} = \beta k_o I_p - \xi_s I_s \quad (12b)$$

where $\xi_s = (\mu/\rho)(H/\kappa)$ is an effective relaxation length as measured in Figure 8 ($= 0.0062 \text{ cm}^2 \cdot \text{g}^{-1}$) and calculated in Figure 2. Thus, substituting Equation 11 into Equation 12b and integrating (where it is assumed that there is no secondary particle intensity at the top of the atmosphere, i.e. $I_s = 0$ at $h = 0$), one obtains:

$$I_s(h) = \beta k_o I_{po} e^{-\xi_s h} \left[\frac{1 - \exp[-(k_o - \xi_s)h]}{k_o - \xi_s} \right] \quad (13)$$

Again, normalising Equation 13 to an atmospheric depth h_o yields the following scaling function (for altitude):

$$f_{Alt}(h) = \frac{I_s(h)}{I_s(h_o)} = \exp[-\xi_s(h - h_o)] \left[\frac{1 - \exp[-(k_o - \xi_s)h]}{1 - \exp[-(k_o - \xi_s)h_o]} \right] \quad (14)$$

The parameter k_o in Equation 14 is fitted to provide a maximum value of the function at the Pfozter maximum, i.e. at an altitude of 20 km or atmospheric depth of $\sim 60 \text{ g} \cdot \text{cm}^{-2}$, yielding a value of $k_o = 0.043 \text{ cm}^2 \cdot \text{g}^{-1}$. This result is consistent with the LUN calculations of Figure 2(a) which show a greater relaxation length for the primary protons near the top of the

atmosphere. Equations 6 and 14 are compared in Figure 10, which reveals that the term in large square brackets in Equation 14 is equal to unity over the range of atmospheric depths in Figure 8. A more complete transport calculation indicates that the Pfozter maximum is somewhat dependent on latitude and the type of particle involved. However, as a first approximation, Equation 14 is able to account for the main features observed in Figures 2 and 10 for the secondary particles including a maximum due to their build-up and an approximate exponential loss in the lower part of the atmosphere.

To account for solar cycle effects, a normalising function for the heliocentric potential was found using the CARI 5E transport code. About 1350 CARI 5E runs were compiled for 23 flights worldwide at six-month intervals over a 28-year period at 10.6 km. The effective dose of each flight was normalised to a heliocentric potential of 650 MV. A correlation was developed to allow for interpolation of U for values from 400 to 1500 MV, where it is observed that there is also a slight dependence on the geomagnetic latitude B_m (in degrees) (which is more pronounced at higher latitudes), such that:

$$f_{Heli}(U, B_m) = \begin{cases} \left[\frac{f_2 - f_1}{25} \right] |B_m| + f_1, & 0 \leq |B_m| < 25 \\ f_2, & |B_m| \geq 25 \end{cases} \quad (15a)$$

where f_1 and f_2 are explicit linear functions of U (in MV):

$$\begin{aligned} f_1(U) &= -1.494 \times 10^{-4}U + 1.1026 \text{ and} \\ f_2(U) &= -3.992 \times 10^{-4}U + 1.2696. \end{aligned} \quad (15b)$$

Here f (as well f_1 and f_2) are normalised to a value of unity at 650 MV.

On further examination of the symmetry around the equator in Figure 9 (with a mirroring of data), it was

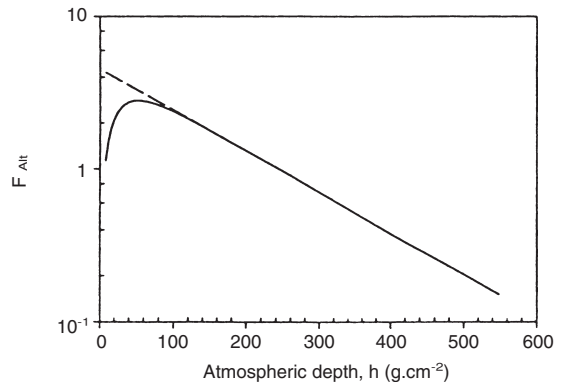


Figure 10. Comparison of the altitude correction function given in Equations 6 (---) and 14 (—).

seen that the north to south symmetry was not exact. This lack of symmetry is due in part to the 10.7° offset of the spin axis of the Earth with respect to the magnetic dipole axis, which gives rise to deviations in the magnetic field (in particular, the South Atlantic Anomaly). In addition, the collected data do not span the full range of geomagnetic coordinates, which limits the ability of the correlation to be a reliable method for interpolating the dose rate for any flight worldwide. To allow for the asymmetries of the Earth's magnetic field, the data can be plotted instead as a function of the vertical cut-off rigidity (Figure 11).

Figure 11 shows that the experimental data from the 36 flights cover all possible values of vertical cut-off rigidity (R_c) from 0 to 16 GV. A correlation of the global dose rate as a function of R_c is therefore possible for a given global position (i.e. geomagnetic latitude B_m). Symmetry was verified by differentiating data collected north of the equator with that south of the equator. The two sets of data overlapped, showing that the relationship of dose rate and R_c (within experimental uncertainties) is symmetrical around the equator and is in fact a better representation than a plot of dose equivalent rate against B_m . The final step was the development of a best-fit polynomial to the data in Figure 11 providing the normalised dose rate \dot{H}_o (in $\mu\text{Sv}\cdot\text{h}^{-1}$) (at 650 MV and 10.6 km) as a function of the vertical cut-off rigidity R_c (in GV):

$$\dot{H}_o = 3.474 \times 10^{-5} R_c^5 - 1.599 \times 10^{-3} R_c^4 + 2.741 \times 10^{-2} R_c^3 - 0.1956R_c^2 + 0.1630R_c + 5.784 \quad (16)$$

Equation 16 is used for the code development to allow for dose rate prediction for any global position, with corrections for the effects of altitude and solar cycle via Equations 14 and 15, respectively, where it can generally be written:

$$\dot{H}(R_c, h, U; B_m) = \dot{H}_o f_{\text{Alt}} f_{\text{Helio}} \quad (17)$$

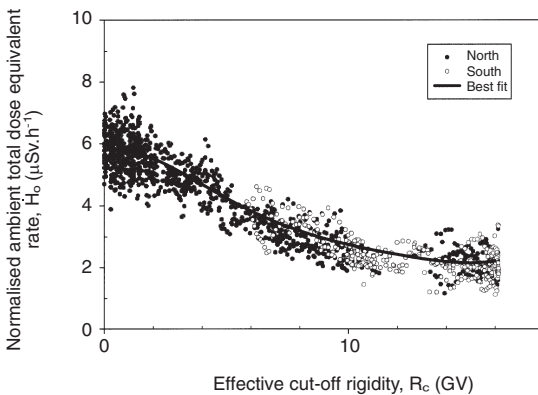


Figure 11. Plot of dose rate \dot{H}_o (normalised to $U = 650$ MV and 10.6 km) against effective vertical cut-off rigidity, R_c (GV). The R_c values were calculated from the Smart-Shea model of Equation 2.

Comparison to PTB measurements

At the PTB in Germany, concurrent measurements have been conducted. In the PTB analysis, measurements with a neutron monitor and an ionisation chamber were summed to produce a total dose equivalent rate (similar to that performed with the bubble detectors and ionisation chamber in Table 4). The instrumentation was flown on 39 flights worldwide⁽¹⁰⁾. The PTB data taken from References 9 and 10 can be compared to the RMC data set by similarly normalising the former data to 10.6 km and 650 MV (using the previous methodology) and plotting the dose equivalent rate against R_c . As seen in Figure 12, both studies are in excellent agreement where the best fit curves for each of the data sets agree within 5%.

Comparison to LUIIN transport code calculations

The RMC and PTB data were also compared to calculations with the radiation transport code LUIIN 2000. LUIIN is a deterministic code based on an analytical two-component solution (i.e. longitudinal and transverse components) of the Boltzmann transport equation that uses the primary nucleon flux at the top of the atmosphere as a boundary condition. The primary flux is derived from the Garcia-Munoz equation below 10 GeV⁽⁵⁵⁾, and the Peters equation for higher energies⁽⁵⁶⁾ as normalised to the Gaisser-Stanev values at 10.6 GeV⁽⁵⁷⁾. The scientific basis of the code is detailed in References 11, 58 and 59. In particular, the code provides for a calculation of the atmospheric cosmic ray angular fluxes, spectra, scalar fluxes and ionisation, and these quantities are then used to calculate the absorbed dose in a semi-infinite 30 cm slab phantom (which provides a simplified representation of the human body in an aircraft). The absorbed dose data at each depth are

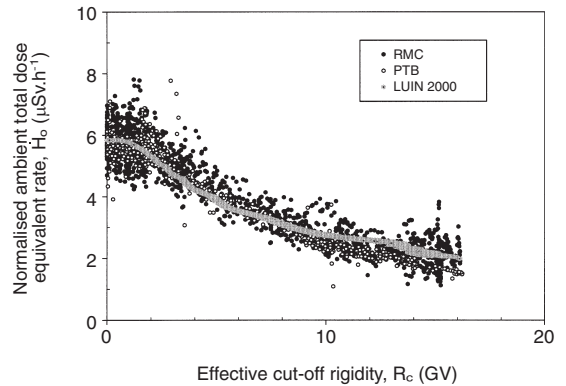


Figure 12. Comparison of the experimental data at RMC and PTB (normalised to $U = 640$ MV and 10.6 km) with the LUIIN 2000 code predictions. The vertical cut-off rigidity values are based on the IGRF 1995 table values for a five degree by five degree world grid.

obtained by integrating the scalar energy spectrum multiplied by the flux-to-dose conversion factors at that depth. Absorbed dose data at various depths are then used to construct absorbed doses for bilateral isotropic exposure⁽⁶⁰⁾. The equivalent dose to bone marrow and skeletal tissue is also calculated at a depth of 5 cm in ICRU tissue. The effective dose calculations are based on flux-to-effective dose conversion coefficients in References 45 and 61 to 65. In addition, LUIIN is able to provide an output in terms of an ambient dose equivalent ($H^*(10)$), using conversion coefficients from ICRP 74. Due to the penetrating nature of the radiation in airline exposure, LUIIN 2000 predicts that the total ambient dose equivalent is very close to the effective dose. However, this result is somewhat different from that suggested in Reference 49 where there is a greater difference between the ambient dose equivalent and effective dose. This latter result primarily arises as a consequence of the two-fold increase in the proton fluence rate in Figure 2(a) with FLUKA compared to that of LUIIN. The LUIIN code has in fact been successfully validated against measured spectral data for the vertical proton flux between 700 g.cm⁻² and sea level⁽⁵⁹⁾. Hence, this discrepancy in the proton fluence will be exacerbated in the calculation of the effective dose as a consequence of a significant radiation weighting factor of 5 for the protons.

In the present analysis, the RMC flights in the experimental database were first simulated for a constant altitude of 10.6 km and 650 MV providing an ambient dose equivalent rate along the entire flight path of each flight (Figure 12). In addition, the actual flight paths were simulated with LUIIN and the correlations of Equations 14 and 15 for altitude and heliocentric potential effects were subsequently applied in order to test the given normalisation procedure, which yielded similar results to that shown in Figure 12. For these comparisons, the data are plotted against the latest vertical cut-off rigidity calculations for the International Geomagnetic Reference Field (IGRF) of 1995. There is again excellent agreement between the experimentally based model and the theoretical (H^*10) LUIIN code predictions (i.e. within

7%). The LUIIN 2000 curve is practically identical to the best-fit polynomial for the proposed curve in Figure 11.

CODE DEVELOPMENT AND VALIDATION

A Predictive Code for Aircrew Radiation Exposure (PC-AIRE) was developed, in a Visual C++ platform, from the data analysis and the equations produced therein⁽⁶⁶⁾. This code was written to be user-friendly and requires minimal time for data input, calculation and data storage. The code requires the user to input the date of the flight, the origin and destination airports, the altitudes and times flown at those altitudes. Look-up tables produce the latitude and longitudes of origin and destination, as well as the heliocentric potential. A great circle route is produced between the two airports, and the latitude and longitude are calculated for every minute of the flight (see Appendix 2)⁽⁶⁶⁾. The vertical cut-off rigidity is calculated from either Equations 2 and 3 (which provide for a 3-epoch average), or interpolated from IGRF-1995 tabulated data for the given geographical coordinates along the flight path. The dose rate is then integrated along the great circle path at one minute intervals using the model of Equation 17, which is based on the normalised correlation in Equation 16 (Figure 11), and unfolded to the actual altitude flown (Equation 14) and the heliocentric potential for the date of the flight (Equation 15). The code outputs the total ambient dose equivalent for the total flight route. The PC-AIRE code was validated against the remaining 26 flights from the original data set collected with the RMC TEPC (i.e. these validation data were independent of the 36-flight data used for model development). As shown in Figure 13, the PC-AIRE predictions of the validation flights are in very good agreement with the TEPC measurements for those flights. Here the measured TEPC data have a relative error of ~18%, while the code, based on a sensitivity analysis, has a predictive error of about 20% (which accounts for the uncertainty due to deviations in the flight path from a great circle route as well as uncertainties in the scaling functions for the altitude and heliocentric potential).

Table 5. Comparison of route doses from previous database (derived from BD measurements) with PC-AIRE predictions.

Grouped global flight region	Sample route	Scheduled flight time	Route dose (μ Sv per flight)	
			Database	PC-AIRE
Trans-Pacific	PEK-CYVR	10h 40min	50 ± 14	55
Trans-Atlantic	CYVR-LHR	9h 6min	43 ± 19	52
Trans-Canada	CYYZ-CYVR	4h 26min	23 ± 6	24
Caribbean	CUN-CYYZ	3h 37min	22 ± 4	15
Northwest/Yukon Territories	CYOW-CYFB	2h 50min	11 ± 4	15
Pacific	MNL-HKG	1h 43min	3 ± 2	3.3

A PC-AIRE prediction of route doses (in units of the ambient total dose equivalent) is shown in Table 5 for representative flights which cover various global flight regions, assuming an altitude of 10.6 km (i.e. atmospheric depth of 243 g.cm⁻²) and a heliocentric potential of 500 MV (which is close to a recent minimum in the solar cycle or a maximum galactic situation). For the non-equatorial regions, these calculations yield a typical dose equivalent rate of ~5.4 μSv.h⁻¹. The ability of the code to extrapolate to supersonic altitudes can be determined with the use of the proposed scaling function in Equation 14. For instance, at 18.2 km (73 g.cm⁻²), Equation 14 (or Figure 10) indicates a factor of $f_{Alt} = 2.7$, yielding an augmented dose rate via Equation 17 of ~15 μSv.h⁻¹. This extrapolated value is in good agreement with the calculations of O'Brien *et al*⁽⁶⁸⁾ which indicate an equivalent dose rate to the bone marrow and skeletal tissue of ~16 μSv.h⁻¹, and a dose equivalent rate of ~19 μSv.h⁻¹ as suggested by Reitz⁽²⁴⁾ for data collected at 55° geomagnetic latitude (during solar minimum conditions). In addition, an extensive measurement campaign was undertaken using the passive dosimetry boxes of the NRPB on 96 return flights (London to New York) on the British Airways Concorde, which yielded an average H*(10) total dose equivalent rate of ~11 μSv.h⁻¹ at 16.1 km (102 g.cm⁻²)⁽⁶⁹⁾. This latter value is also in good agreement with a predicted PC-AIRE value of ~12 μSv.h⁻¹ at this slightly lower altitude. Thus, there is some confidence in the ability of the model to extrapolate to supersonic altitudes. This capability is expected considering the well characterised relaxation length in Figure 8, and the essentially simple exponential behaviour of the dose rate as a function of atmospheric depth (Figures 2 and 10) over the given range of altitude for these various types of commercial flights.

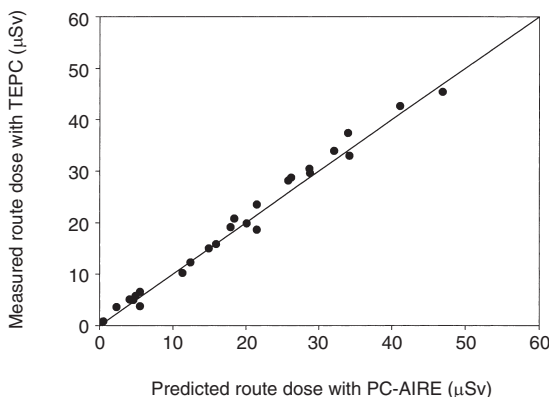


Figure 13. Plot of measured TEPC results versus PC-AIRE Code predictions of flight dose.

AIRCREW ANNUAL EXPOSURE PREDICTION

An extensive study was previously carried out with only bubble detectors to measure the neutron dose equivalent on over 385 different Canadian-based flight routes⁽²⁾. These measurements were then scaled to a total dose equivalent for the given route with the use of a neutron fraction. The neutron fraction was derived from equivalent dose calculations with CARI-LF, which were further supported by a single scientific flight using a variety of active (i.e. TEPC, extended range neutron rem meter, and ionisation chamber) and passive (i.e. BD and TLDs) instrumentation. From this analysis, a database was constructed under a Microsoft Access platform to provide a look-up of the total dose equivalent for a given flight route. Using this extensive database program, with the actual flight schedules of several aircrew (pilots and flight attendants) supplied by the various air carriers, an estimate of the annual exposure of the individual aircrew was obtained.

The PC-AIRE code was further used to simulate these flights to provide a prediction of the annual aircrew exposure. Unfortunately, the previously developed database does not correlate the route flight parameters (i.e. altitude) to a specific flight dose. As such, an average altitude of 10.6 km and a heliocentric potential of 500 MV (corresponding to the previous study period) were assumed for the simulation. A comparison of six selected flights, which cover different global regions, is shown in Table 5. In general, PC-AIRE is typically ~15% higher than that derived from the database program. This result is principally attributed to the use of an older calibration factor for the bubble detectors (see section on bubble detector calibration) and a slight difference in the neutron fraction between the theoretical CARI-LF predictions and that obtained from the measured BD/TEPC ratio in Table 4. As such, the PC-AIRE predictions of the annual aircrew exposure (as shown in Figure 14) are ~15% higher than that reported in Reference 2. As expected, all but one aircrew member surpassed the proposed ICRP 60 public limit of 1 mSv.y⁻¹, whereas all crew members are well below the

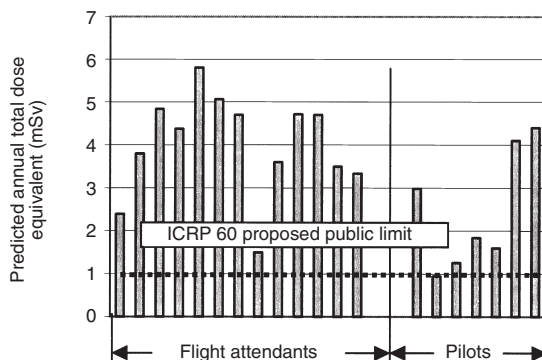


Figure 14. PC-AIRE prediction of aircrew annual exposure.

proposed occupational limit of $20 \text{ mSv}\cdot\text{y}^{-1}$. These data, in conjunction with Table 1, demonstrate that there is a valid requirement to monitor the radiation exposure of aircrew, perhaps using such predictive tools as that developed in this work.

It is important to recall that the quantity being determined in the proposed PC-AIRE code is the ambient dose equivalent, whereas legal regulation limits are in terms of effective dose. For typical terrestrial situations, the ambient dose equivalent is a reasonable surrogate for the effective dose since it is a more conservative quantity. However, as suggested in Reference 49, the ambient dose equivalent may no longer be a conservative estimate of the effective dose for the complex high energy cosmic spectrum, primarily due to the enhanced weighting factor of 5 for the protons. This result can be clearly seen in Figure 15(a), where the

ratio of effective dose (E) to ambient dose equivalent ($H^*(10)$) is greater than unity based on the FLUKA analysis in References 49 and 70. On the other hand, the current LUN calculations in Figure 15(b) suggest that $E/H^*(10)$ is typically closer to unity as a consequence of the lower proton fluence rate in Figure 2(a). Consequently, in the PC-AIRE code, an effective dose calculation is performed where the user has a choice of scaling function as depicted in Figures 15(a) and (b), such that

$$f_{E/H^*(10)}^{\text{FLUKA}}(A, R_c) = \begin{cases} \frac{(f_2 - f_1)}{12} R_c + f_1, & 0 \leq R_c < 12 \\ f_2, & R_c \geq 12 \end{cases} \quad (18a)$$

where

$$f_1 = 0.9797 + 9.427 \times 10^{-3} A + 1.3635 \times 10^{-3} A^2$$

and

$$f_2 = 0.9973 + 8.6025 \times 10^{-3} A + 7.2967 \times 10^{-4} A^2,$$

and

$$f_{E/H^*(10)}^{\text{LUN}}(A, R_c) = 9.901 \times 10^{-3} A + f_3(R_c) \quad (18b)$$

where

$$f_3 = -4.170 \times 10^{-4} R_c^2 + 1.188 \times 10^{-2} R_c + 0.8816.$$

In Equations 18a and 18b, A is the altitude in km and R_c is the vertical cut-off rigidity in GV. These correlations are derived with the use of Lagrange interpolation polynomials and correspond to conditions near a solar minimum. Thus, the ambient dose equivalent rate in Equation 17 is multiplied by the chosen conversion function in Equations 18a or 18b to yield an effective dose, where Equation 18a will yield the more conservative estimate (i.e. by $\sim 20\%$ at subsonic altitudes). As a caveat, the LUN predictions of ambient dose equivalent have been validated against two independent data sets in Figure 12 based on an extensive series of in-flight measurements. However, as mentioned in the derivation of Equation 4, the proton contribution will result in only a small (i.e. approximately 10%) enhancement of the dose equivalent from the absorbed dose value if one employs a standard Q(LET) relationship in such calculations. As such, the ambient dose equivalent estimates of FLUKA and LUN should not vary significantly, although further investigation is clearly warranted to improve upon the effective dose calculation in order to reduce the observed discrepancy in Figure 15 between the two codes. This further investigation is important since an overly conservative estimate of effective dose could result in undue restrictions if such theoretically based tools are used to manage the aircrew exposure.

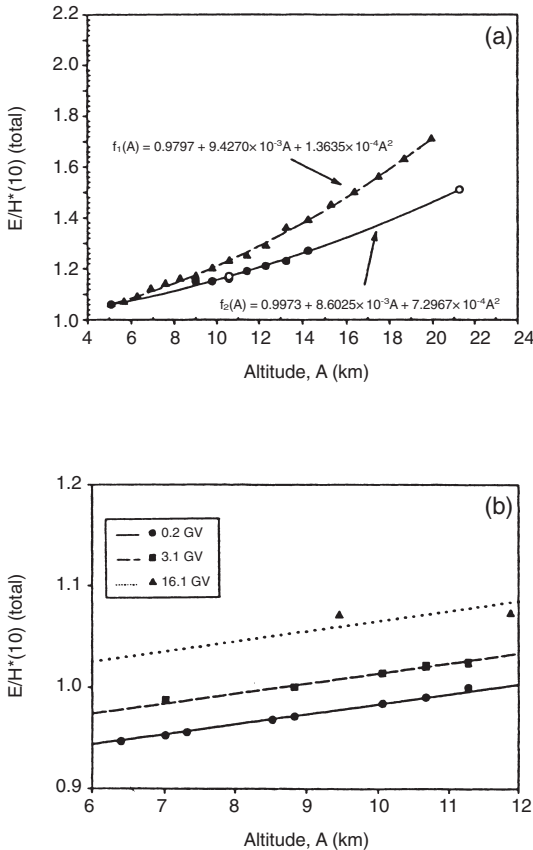


Figure 15. Conversion factor from ambient dose equivalent to effective dose as derived from (a) FLUKA at solar minimum and (b) LUN calculations at 650 MV. The lines in (b) are derived from Equation 18b. In (a) (●) 17.8 GV (10°N – 91°E), Reference 49, Table 7. (○) 12.0 GV (35°N – 137°E), Reference 49, Table 3. (—) Best fit polynomial (12.0 to 17.6 GV). (▲) 0.4 GV, Reference 70. (---) Best fit polynomial (0.4 GV).

CONCLUSIONS

- (1) A tissue-equivalent proportional counter (TEPC) was utilised to conduct an extensive in-flight measurement programme to investigate aircrew radiation exposure at jet aircraft altitudes over a one-year period. Over 20,000 total (ambient) dose equivalent rate results were collected on 62 world-wide flights, spanning altitudes up to 12.4 km, and geomagnetic latitudes from 50° south to 85° north that cover the complete cut-off rigidity of the Earth's magnetic field. This database compared extremely well to other data collected by the PTB on different flights, utilising different instruments and a contrasting research methodology (where ionisation chamber and neutron rem meter data were summed to yield the same total dose equivalent). The current data were also successfully compared to theoretical transport calculations with the LUIN 2000 computer code. Thus, these experiments provide for a validation of the deterministic LUIN code for a prediction of the total (ambient) dose equivalent received by aircrew. On the other hand, the results from the two independent laboratories can be used to produce a single (experimentally based) function (item 2), which can be easily adapted as a practical code (item 3) for aircrew radiation exposure assessment.
- (2) A semi-empirical model was developed to relate the measured total (ambient) dose equivalent rate to the vertical cut-off rigidity (which is a function of the latitude and longitude). This correlation was obtained by relating the dose rate data to specific positional information as a function of time along the flight path of the aircraft. The TEPC data were summed and smoothed to minimise the data uncertainty (~18% relative error) without an undue loss of data. Physically based functions were developed to scale the dose rate data as a function of altitude (using a measured relaxation length of 0.0062 g.cm⁻²) and heliocentric potential (based on a theoretical analysis with CARI 5E). The current model therefore provides for an estimate of the total (ambient) dose equivalent rate for any global flight path and time in the solar cycle.
- (3) The model was developed into a computer code, PC-AIRE, for global dose prediction using a great circle route calculation (e.g. between various waypoints or the departure and arrival airport locations) by summing the dose rates over the given flight path. The code methodology was directly validated against an independent set of TEPC route-dose measurements on 26 flights. An effective dose calculation is also possible with PC-AIRE using conversion functions developed from an analysis with LUIN and FLUKA, but further work is needed to improve upon the discrepancy of ~20% for the ratio

of the effective dose to ambient dose equivalent as obtained between the two transport codes.

- (4) An assessment of the annual exposure of Canadian-based aircrew was performed with the PC-AIRE code using actual flight frequency information. From this analysis, most aircrew will exceed the annual ICRP 60 public limit (1 mSv.y⁻¹), but are well below the proposed ICRP 60 occupational limit (20 mSv.y⁻¹).

ACKNOWLEDGEMENTS

The authors would like to thank J. Servant of Transport Canada and Dr S. Kupca and C. Thorp of the Director General Nuclear Safety (DGNS) of the Department of National Defence for their assistance in this study. The authors would like to express their gratitude to the employees and management of Air Canada, First Air and British Airways for their assistance and cooperation in the arrangement for measurements on board commercial flights. In particular, the authors wish to thank Capt. J. Nakielny, Capt. C. J. Saint-Martin and Dr C. Thi-beault of Air Canada, J. Lafrance of First Air and D. Irvine of British Airways. The authors would also like to thank 1 Canadian Air Division of the Canadian Forces, Air Operations at 8 Wing Trenton and the crew-members of 437, 436 and 429 Squadrons for their cooperation and assistance in data collection on board military flights. The authors would also like to acknowledge the help of Dr M. Silari and A. Mitaroff at CERF, B. Ellaschuk at RMC, and Dr T. Cousins and J. R. Brisson of the Defence Research Establishment Ottawa, and Dr D. T. Bartlett of the National Radiological Protection Board, for the use of their passive dosimeter systems and for the analysis of these results. Financial support for this study was received from Transport Canada and DGNS.

APPENDIX 1

Instrument calibration*TEPC (external source calibration)*

Before using the TEPC to monitor radiation at jet altitudes, it is necessary to know the response of the TEPC relative to the ambient dose equivalent, H*(10). In other words, the TEPC must be calibrated in a known field of interest in order to obtain a multiplication factor, *f*, which can be applied to H_{TEPC} such that⁽³³⁾

$$H^*(10) = fH_{\text{TEPC}} \quad (\text{A1.1})$$

The response of the TEPC was compared to H*(10) in polyenergetic neutron reference fields (²⁵²Cf and AmBe) and in monoenergetic neutron beams at the PTB. The results from the polyenergetic neutron fields are given in

Table A1.1, while the results from the mono-energetic neutron beam measurements are shown in Figure A1.1.

These measurements show that H_{TEPC} is systematically higher than $H^*(10)$ by an average of $\sim 15\%$ (excluding the measurement at a neutron energy of 0.144 keV, where the TEPC is known to under-respond since the range of the recoil proton is less than the TEPC diameter)^(31,34). In addition, comparison to a calibrated ^{137}Cs gamma source shows that the TEPC over-responds to gamma rays by approximately 10%. Based on these various results, f in Equation A1.1 is taken as $1/1.15 = 0.87$.

TEPC (internal alpha source calibration)

The TEPC also contains an internal alpha source (i.e. ^{244}Cm) which can be used for calibration since the cosmic ray spectrum also contains particles of higher LET. Thus, the value of f in Equation A1.1 can also be confirmed by examining the position of the peak generated by the internal source. This source emits 5.8 MeV alpha particles with virtually no gamma rays⁽³⁵⁾. The stopping power (S/ρ) of these particles in the detector can be evaluated with a Monte Carlo analysis using the SRIM-2000 code, assuming an atomic composition of: H (10.3 wt%), C (56.9 wt%), N (3.5 wt%) and O (29.3 wt%) for the muscle-equivalent (propane) gas of density $\rho = 1.68 \times 10^{-5} \text{ g.cm}^{-3}$ (at 20°C and 933 Pa (7 torr))⁽³⁴⁾. The SRIM calculation indicates a very large range of $\sim 2.5 \text{ m}$ in the low density gas⁽³⁶⁾. As such, the high energy alpha particle should not slow down very much as it passes through the detector sphere (of diameter $d_d = 12.7 \text{ cm}$). This can be further demonstrated with a simple energy-range calculation. The energy loss of the particle as it traverses through the gas is given by:

$$-dE/dx = S \quad (\text{A1.2})$$

From the SRIM analysis, it can be seen that the stopping power is relatively constant for a high energy alpha particle (i.e. until it has slowed down and is near the end of its range), where $(S/\rho) \sim 856 \text{ MeV.cm}^{-2}.\text{g}^{-1}$, or $S = 0.0146 \text{ MeV.cm}^{-1}$ ⁽³⁶⁾. Equation A1.2 can therefore be directly integrated to yield:

$$E(x) = -Sx + E_o \quad (\text{A1.3})$$

where $E_o (= 5.8 \text{ MeV})$ is the initial energy of the alpha particle. The average energy of the particle must be evaluated over a mean chord length of the spherical detector, $\bar{\ell} = (2/3)d_d$, where on use of Equation A1.3:

$$\langle E \rangle = \frac{\int_0^{\bar{\ell}} E(x) dx}{\int_0^{\bar{\ell}} dx} = E(\bar{\ell}/2) \quad (\text{A1.4})$$

Equations A1.3 and A1.4, with the above parametric values, yield an average energy in the detector sphere of $\langle E \rangle = 5.7 \text{ MeV}$, which is close to the initial energy E_o .

It is possible to determine the amount of energy imparted to the counter gas using the relation

$$\epsilon = (S/\rho)\rho_t d_t \quad (\text{A1.5})$$

Hence, with an $(S/\rho) \sim 856 \text{ MeV.cm}^2.\text{g}^{-1}$, a tissue site density $\rho_t = 1 \text{ g.cm}^{-3}$ and tissue sphere diameter, $d_t = 2 \mu\text{m}$, the energy imparted by the 5.8 MeV alpha particle in the current detector cavity is $\epsilon = 171 \text{ keV}$. This value is in excellent agreement with that reported in the literature (i.e. 170 keV for a $2 \mu\text{m}$ site size)⁽³⁷⁾. From the definition of the lineal energy y

$$y = \epsilon/\bar{\ell} \quad (\text{A1.6})$$

where, for the simulated tissue site, the mean chord length $\bar{\ell} = (2/3) d_t$ it follows that

$$y = 1.5(\epsilon/d_t) \quad (\text{A1.7})$$

A lineal energy peak is therefore predicted to occur with Equation A1.7 at a value of $128 \text{ keV}.\mu\text{m}^{-1}$. The actual spectrum measured by the TEPC consists of a single peak with a maximum near $148 \text{ keV}.\mu\text{m}^{-1}$ (consistent with an original calibration by the manufacturer to a peak position of $150 \text{ keV}.\mu\text{m}^{-1}$). Thus, this actual peak occurs at a lineal energy which, again, is $\sim 15\%$ higher than that predicted by theory ($128 \text{ keV}.\mu\text{m}^{-1}$). The absorbed dose calculation will be directly affected by this same factor, which further supports the use of the proposed value of f in Equation A1.1.

Comparison to the HANDI TEPC at CERN

The TEPC was also compared to a HANDI TEPC with a cross comparison measurement of the integral field at CERN (which simulates a high energy cosmic neutron spectrum as depicted in Figure 4). The HANDI TEPC typically yielded a total ambient dose equivalent which was $\sim 20\%$ higher as compared to the TEPC measurement after using the correction factor derived in the external and internal calibration studies. However, the use of independent combined instrumentation suites in both the RMC and PTB investigations (see for example the section on at-altitude measurements) further support the current TEPC calibration and its ability to measure both the low and high LET components of the complex cosmic ray field at altitude.

Bubble detectors

In an earlier study, BDs were used to measure the dose equivalent of cosmic neutrons⁽²⁾. These measurements were subsequently scaled to a total dose equivalent (i.e. for all particle types) using an estimate of the neutron fraction based on CARI-LF equivalent dose calculations. The present study, however, also provided a unique opportunity to determine experimentally the scale factor from the ratio of the BD/TEPC measurement. This type of evaluation is particularly important

since simple passive, direct-reading BDs can alternatively be used to measure the high LET component of the at-altitude field, which can be easily scaled to yield a total dose equivalent without the need for sophisticated instrumentation. Therefore, for this analysis, the BDs were also calibrated in ground-based accelerator studies using the monoenergetic neutron source at the PTB and subsequently validated in an integral reference field at the CERF facility that simulates the cosmic neutron spectrum (Figure 4).

For the bubble detectors, a response-to-dose equivalent calibration factor, RD_{amb} , can be determined experimentally by taking the ratio of the integral response of the detector (i.e. the number of bubbles, M) to the dose equivalent produced in a known reference field, H :

$$RD_{amb} = M/H \quad (A1.8)$$

This calibration factor (once determined) can be used to convert the number of bubbles produced by an unknown radiation field, M_u , into a measured (ambient) neutron dose equivalent, DE_n :

$$DE_n = \frac{M_u}{RD_{amb}} \quad (A1.9)$$

Alternatively, a theoretical RD_{amb} can be calculated for an ideal neutron detector⁽⁹⁾:

$$RD_{amb} = \frac{\int R_\phi(E)\phi(E)dE}{\int h(E)\phi(E)dE} \quad (A1.10)$$

which requires a knowledge of the energy response function of the detector, $R_\phi(E)$; the shape of the cosmic neutron energy spectrum, $\phi(E)$; and the conversion factor, $h(E)=H^*(10)/\Phi$, between the ambient dose equivalent $H^*(10)$ and neutron fluence Φ . The energy response function of the detector, including the more recent PTB data, is shown in Figure A1.2. For this analysis, the combined $H^*(10)/\Phi$ operational coefficients of Siebert *et al* (for neutron energies below 200 MeV) and Sannikov *et al* (for neutron energies above 200 MeV) shown in Figure A1.3 can be employed⁽³⁸⁻⁴⁰⁾. Thus, an ideal calibration factor can be evaluated from Equation A1.10 with a further knowledge of the neutron spectrum. The results of this calculation are shown in Table A1.2 using the various spectra in Figure 4, which include: (i) an actual measurement by Goldhagen (atmospheric

depth of 222 g.cm⁻²) with a multisphere neutron spectrometer^(2,41); (ii) a Monte Carlo calculation with the FLUKA code by Roesler (atmospheric depth of 200 g.cm⁻²)⁽²⁸⁾; and (iii) a simulated spectrum measured on top of the concrete accelerator shielding at CERF^(42,43). For neutron energies less than 1 eV, the theoretical calculations of Armstrong have been

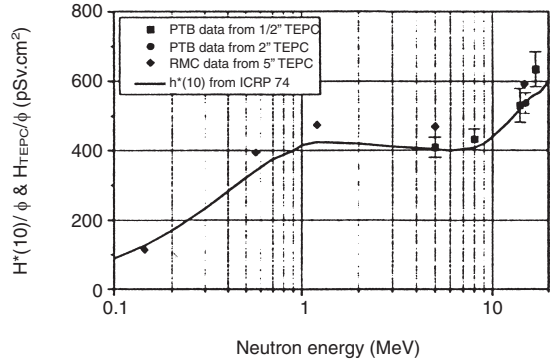


Figure A1.1 Response of RMC TEPC compared to $H^*(10) \Phi$ at selected neutron energies. The response of the RMC TEPC, H_{TEPC}/Φ , is compared to $H^*(10)/\Phi$ values given in ICRP 74 (solid line). Responses of PTB-owned TEPCs are also shown for comparison.

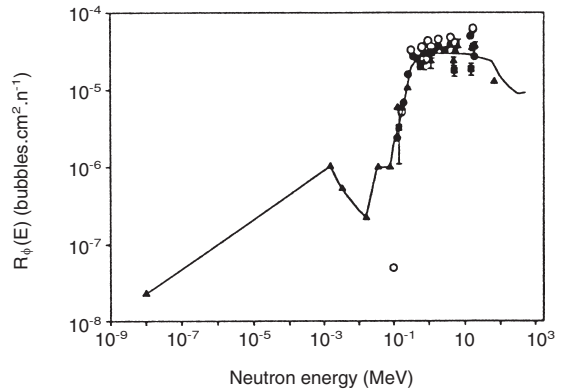


Figure A1.2. Bubble detector response-to-fluence function (for a detector with unit sensitivity of 0.1 bubbles.μSv⁻¹). (●) Noulty⁽⁷¹⁾, (○) Noulty⁽⁷¹⁾, (▲) Tume *et al*⁽⁷²⁾, (■) PTB measurements (2000), (—) proposed functions.

Table A1.1. Response of RMC TEPC to polyenergetic neutron reference fields.

Source	Reference ($H^*(10)$) dose rate ($\mu\text{Sv.h}^{-1}$)	Measured dose rate ^(a,b) ($\mu\text{Sv.h}^{-1}$)	Relative difference (%)
²⁵² Cf	996 ± 24	1165	16.9
Am(Be)	11.8 ± 0.6	14.2	20.6

^(a) For $\gamma > 10 \text{ keV.}\mu\text{m}^{-1}$ (neutrons only).

^(b) Corrected for backscattering (using shadow cone).

pinned to the measured spectrum of Goldhagen and the calculated one with FLUKA in Figure 4⁽⁴⁴⁾. As expected, the calculated value of RD_{amb} in Table A1.2 does not vary much with these comparable spectra. A response-to-effective dose calibration factor, RD_{eff} , can also be similarly obtained in Table A1.2 for the BD by replacing the quantity $H^*(10)/\Phi$ in Equation A1.10 with the neutron fluence-to-effective dose conversion coefficients E/Φ of Figure A1.3⁽⁴⁵⁾. Hence, the ambient dose equivalent, as measured with the bubble detector for a cosmic neutron spectrum, will provide a somewhat conservative estimate of the effective dose (as seen by replacing RD_{amb} by RD_{eff} in Equation A1.9).

Thus, in the current study, the calibration factor RD_{amb} is evaluated from Equation A1.10 for the cosmic neutron spectrum of Goldhagen (Table A1.2), yielding a value of $RD_{amb} = 3.8 \text{ bubble} \cdot \mu\text{Sv}^{-1}$. (This calibration factor specifically corresponds to a detector with a sensitivity of $5.6 \text{ bubbles} \cdot \mu\text{Sv}^{-1}$ for an AmBe neutron spectrum and ICRP $H^*(10)/\Phi$ conversion coefficients.)

With a knowledge of this factor, the neutron dose equivalent can be easily evaluated with Equation A1.9 by simply counting the number of bubbles (M_b) on a given flight. No correction has been considered for the interaction of high energy protons with the neutron bubble detectors since this effect is well within the measurement uncertainty of the detector. In particular, the particle fluence rate is an order of magnitude less for protons compared to neutrons at typical aircraft altitudes (see for example Figure 2), and the response of the bubble detectors to high energy protons is somewhat reduced from that for neutrons, as observed in accelerator experiments at TRIUMF.

In order to confirm experimentally this calculated value of RD_{amb} for an ideal detector, an experimental calibration was made on top of the concrete shielding at CERF. As mentioned previously, the neutron spectrum generated behind the accelerator shielding provides a reasonable simulation of the neutron spectrum at aircraft altitudes (Figure 4). A measured experimental response, M , was made with the bubble detectors for the integral field and compared to the actual neutron dose equivalent, H , as measured with an in-house LINUS (Long Interval NeUtron Survey meter) extended range counter. Thus, using Equation A1.8, an experimental ratio of M/H yielded a value of $RD_{amb} = 3.8 \pm 0.8 \text{ bubble} \cdot \mu\text{Sv}^{-1}$. This value is in excellent agreement with the corresponding value of $3.7 \pm 0.8 \text{ bubble} \cdot \mu\text{Sv}^{-1}$ reported in Table A1.2 for the CERF spectrum.

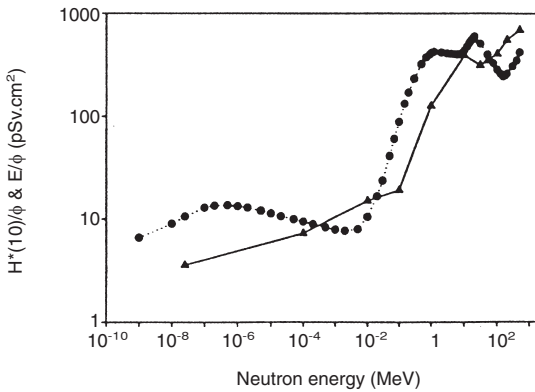


Figure A1.3. $H^*(10)/\Phi$ and effective dose E/Φ conversion coefficients for neutrons. (\blacktriangle) E , (Ferrari 1997)⁽⁴⁵⁾, (\bullet) $H^*(10)$ (Siebert 1995⁽³⁸⁾, Sannikov 1997)⁽⁴⁰⁾.

Table A1.2. Calculated response-to-dose (RD) conversion factors for BDs at 20°C^(a).

Spectrum	Goldhagen ^(b)	FLUKA ^(b)	CERF
RD_{amb} (bubble $\cdot \mu\text{Sv}^{-1}$)	3.8	3.7	3.7
RD_{eff} (bubble $\cdot \mu\text{Sv}^{-1}$) ^(c)	5.9	4.9	4.6

^(a)Calibration factor for a detector with a nominal sensitivity of $6 \text{ bubbles} \cdot \mu\text{Sv}^{-1}$ as calibrated by the manufacturer using an AmBe neutron spectrum and NCRP 38 units (i.e. the $R_\phi(E)$ in Figure A1.2 has been multiplied by a factor of 60 since the latter curve pertains to a detector with a $0.1 \text{ bubble} \cdot \mu\text{Sv}^{-1}$ sensitivity).

^(b)Includes the theoretical spectrum of Armstrong in Reference 44 for thermal neutrons.

^(c)For isotropic (ISO) geometry.

APPENDIX 2

Great circle calculation

An aircraft normally flies a great circle arc (or route), which is the shortest distance between the two points on the surface of a sphere. The total great circle distance (D) between the point of origin, a , and the final destination, b , is⁽⁶⁷⁾:

$$\cos(D) = \sin[A_{lat}] \sin[B_{lat}] + \cos[A_{lat}] \cos[B_{lat}] \cos[A_{lon} - B_{lon}] \quad (\text{A2.1})$$

where D is in radians, and the parameters $A_{lat} = \text{lat}(a)$ and $B_{lat} = \text{lat}(b)$ correspond to the latitude, and $A_{lon} = \text{lon}(a)$ and $B_{lon} = \text{lon}(b)$ correspond to the longitude, of points a and b , respectively. The distance D (rad) can be converted to nautical miles (nmi) where $D(\text{nmi}) = D(\text{rad})(180 \cdot 60) / \pi$.

In order to determine the coordinates of the flight path on a great circle arc at a given distance D (rad) (for a given aircraft speed and time on this path), the following equation is employed:

$$\text{lat} = \text{asin}[\sin[A_{lat}] \cos(D) + \cos[A_{lat}] \sin(D) \cos(t_c)] \quad (\text{A2.2a})$$

$$\text{lon} = \text{mod}\{A_{lon} - d_{lon} + \pi, 2\pi\} - \pi \quad (\text{A2.2b})$$

where

$$d_{\text{lon}} = \text{atan2}\{\sin(t_c)\sin(D)\cos[A_{\text{lat}}], \cos(D) - \sin[A_{\text{lat}}]\sin(\text{lat})\}$$

$$t_c = \text{mod}(\text{atan2}\{\sin[A_{\text{lon}} - B_{\text{lon}}]\cos[B_{\text{lat}}],$$

$$\cos[A_{\text{lat}}]\sin[B_{\text{lat}}]$$

$$- \sin[A_{\text{lat}}]\cos[B_{\text{lat}}]\cos[A_{\text{lon}} - B_{\text{lon}}], 2\pi)$$

The $\text{atan2}(y,x)$ function is the arc tangent of y/x , which is a standard function used in most programming

languages, and $\text{mod}(y,x)$ is the modular function. These equations can therefore be used to calculate the path, distance and position along the path at a given time throughout the flight (with a knowledge of the total flight time and great circle distance D or alternatively the aircraft velocity). This positional latitude and longitude information can then be used to calculate a corresponding geomagnetic latitude (B_m) and, hence, a cutoff rigidity using Equations (2) and (3).

REFERENCES

1. International Commission on Radiological Protection. *1990 Recommendations of the International Commission on Radiological Protection*. ICRP Publication **60** (Oxford: Pergamon Press) (1991).
2. Lewis, B. J., Tume, P., Bennett, L. G. I., Pierre, M., Green, A. R., Cousins, T., Hoffarth, B. E., Jones, T. A. and Brisson, J. R. *Cosmic Radiation Exposure on Canadian-Based Commercial Airline Routes*. Radiat. Prot. Dosim. **86**(1), 7–24 (1999).
3. Sont, W. N. and Ashmore, J. P. *1999 Report on Occupational Radiation Exposures in Canada*. Environmental Health Directorate, 99-EHD-239 (1999).
4. Courades, J.-M. *European Legislation on Protection Against Cosmic Radiation*. Radiat. Prot. Dosim. **86**(4), 343–346 (1999).
5. Barish, R. J. *Health Physics and Aviation: 1990–1994*. Health Phys. **69**(4), 538–542 (1995).
6. Federal Aviation Administration. *Crewmember Training on In-flight Radiation Exposure*. US Department of Transportation, FAA Advisory Circular 120–61 (1994). (Available from the National Technical Information Service, Springfield, Virginia.)
7. *Measures for Managing Exposure to Cosmic Radiation of Employees Working On-Board Aircraft*. Commercial and Business Aviation Advisory Circular, Transport Canada, March 2000 (draft).
8. Green, A. R., McCall, M. J., Lewis, B. J. and Bennett, L. G. I. *Cosmic Radiation Exposure of Aircrew*. Report to Transport Canada, RMC-CCE-NSE-00–02 v.1, Royal Military College (March 2000).
9. Schrewe, U. J. *ACREM — Air Crew Radiation Exposure Monitoring: Summary of Results from Calibrations and TEPC Measurements*. PTB-6.31–1999–2 (Physikalisch Technische Bundesanstalt, Braunschweig, Germany) (October 1999).
10. Schrewe, U. J. *Radiation Exposure Monitoring in Civil Aircraft*. Nucl. Instrum. Methods Phys. Res. A, **422**, 621–625 (1999).
11. O'Brien, K., Friedberg, W., Sauer, H. S. and Smart, D. F. *Atmospheric Cosmic Rays and Solar Energetic Particles at Aircraft Altitudes*. Environ. Int. **22**, (Suppl. 1), S9-S44 (1996).
12. Gaisser, T. K. *Cosmic Rays and Particle Physics* (Cambridge: Cambridge University Press) (1990).
13. Simpson, J. A. *Elemental and Isotopic Composition of the Galactic Cosmic Rays*. Ann. Rev. Nucl. Part. Sci. **33**, 323–381 (1983).
14. Wilson, J. W., Nealy, J. E., Cucinotta, F. A., Shinn, J., Hajnal, F., Reginatto, M. and Goldhagen, P. *Radiation Safety Aspects of Commercial High Speed Flight Transportation*. NASA Technical Paper 3524 (May 1995).
15. Heinrich, W., Roesler, S. and Schraube, H. *Physics of Cosmic Radiation Fields*. Radiat. Prot. Dosim. **86**(4), 253–258 (1999).
16. O'Brien, K. and de P. Burke, G. *Calculated Cosmic Neutron Monitor Response to Solar Modulation of Galactic Cosmic Rays*. J. Geophys. Res. **78**, 3013 (1973).
17. Goldhagen, P. *Overview of Aircraft Radiation Exposure and Recent ER-2 Measurements*. Submitted to NCRP Proc. No 20, Cosmic Radiation Exposure of Airline Crews, Passengers and Astronauts, New York, N.Y. (1999).
18. Wilson, M. Bartol Research Institute, and Vashenyuk, E. Polar Geophysical Institute, Russia, in <http://www.cami.jccbi.gov/aam-600/610/600radio.html>.
19. The sunspot number is compiled by the US National Oceanic and Atmospheric Administration in http://www.ssl.msfc.nasa.gov/ssl/pad/solar/greenwch/spot_num.txt. These numbers published in this table are the monthly averages (SSN) and standard deviation (DEV) derived from the International Sunspot Numbers.
20. Climax counting rate data obtained from the Solar and Upper Atmosphere Group, National Geophysical Data Center, National Oceanic and Atmospheric Administration, Boulder, Colorado (<http://www.ngdc.noaa.gov>)
21. Hayakawa, S. *Cosmic Ray Physics: Nuclear and Astrophysical Aspects* (New York: Wiley and Sons) (1969).
22. Shea, M. A., Smart, D. F. and Gentile, L. C. *Estimating Cosmic Ray Vertical Cutoff Rigidities as a Function of the McIlwain L-parameter for Different Epochs of the Geomagnetic Field*. Phys. Earth Planet. Inter. **48**, 200–205 (1987).
23. Tascione, T. F. *Introduction to the Space Environment* (Malabar, Florida: Orbit Book Co.) (1988).
24. Reitz, G. *Radiation Environment in the Stratosphere*. Radiat. Prot. Dosim. **48**(1), 5–20 (1993).
25. O'Brien, K. and McLaughlin, J. E. *The Radiation Dose to Man from Galactic Cosmic Rays*. Health Phys. **22**, 225–232 (1972).
26. O'Brien, K. *LWIN, A Code for the Calculation of Cosmic Ray Propagation in the Atmosphere*. (update of HASL-275), EML-338 (1978).

AIRCREW EXPOSURE FROM COSMIC RADIATION

27. Aarnio, P. A., Fasso, A., Ferrari, A., Möhring, H.-J., Ranft, J., Sala, P. R., Stevenson, G. R. and Zazula, J. M. *FLUKA: Hadronic Benchmarks and Applications*. In: Proc. Int. Conf. on Monte Carlo Simulation in High Energy and Nuclear Physics, MC'93, Tallahassee, FL, 1993 (Eds. P. Dragovitsch, S.L. Linn and M. Burbank), pp. 88–92 (Singapore: World Scientific) (1994).
28. Roesler, S., Heinrich, W. and Schraube, H. *Calculation of Radiation Fields in the Atmosphere and Comparison to Experimental Data*. Radiat. Res. **149**, 87–97 (1998).
29. Badhwar, G. D. *The Radiation Environment in Low-Earth Orbit*. Radiat. Res. **148**, 3–10 (1997).
30. Green, A. R., Lewis, B. J., Bennett, L. G. I., Pierre, M. and Cousins, T. *Commercial Aircrew Radiation Dosimetry using a Tissue Equivalent Proportional Counter*. In: Proc. 20th Annual Conf. Canadian Nuclear Society, Montreal, Quebec, 30 May–2 June 1999.
31. Waker, A. J. *Principles of Experimental Microdosimetry*. Radiat. Prot. Dosim. **61**, 297–308 (1995).
32. International Commission on Radiation Units and Measurements. *The Quality Factor in Radiation Protection*. ICRU Publication 40 (April 1986).
33. Nunes, J. C., Waker, A. J. and Arneja, A. *Neutron Spectrometry and Dosimetry in Specific Locations at Two CANDU® Power Plants*. Radiat. Prot. Dosim. **63**(2), 87–104 (1996).
34. International Commission on Radiation Units and Measurements. *Microdosimetry*. ICRU Report 36 (Bethesda, Maryland ICRU Publications) (December 1983).
35. Lederer, C. M. and Shirley, V. S. *Table of Isotopes: Seventh Edition* (New York: John Wiley & Sons) (1978).
36. Biersack, J. P. and Ziegler, J. F. SRIM-2000 computer code (v. 9) (1998).
37. Schrewe, U. J., Brede, H. J., Pihet, P. and Menzel, H. F. *On the Calibration of Tissue-Equivalent Proportional Counters with Built-In α Particle Sources*. Radiat. Prot. Dosim. **33**(1–4), 249–252 (1988).
38. Siebert, B. R. L. and Schuhmacher, H. *Quality Factors, Ambient and Personal Dose Equivalent for Neutrons Based on the New ICRU Stopping Power Data for Protons and Alpha Particles*. Radiat. Prot. Dosim. **58**(3), 177–183 (1995).
39. Schuhmacher, H. and Siebert, B. R. L. *Quality Factors and Ambient Dose Equivalent for Neutrons Based on the New ICRP Recommendations*. Radiat. Prot. Dosim. **40**(2), 85–89 (1992).
40. Sannikov, A. and Savitskaya, E. N. *Ambient Dose Equivalent Conversion Factors for High Energy Neutrons Based on the ICRP 60 Recommendations*. Radiat. Prot. Dosim. **70**(1–4), 383–386 (1997).
41. Goldhagen, P. (Environmental Measurements Laboratory of the United States Department of Energy) Private communication (March 1998).
42. *Study of Radiation Fields and Dosimetry at Aviation Altitudes*. Final Report for European Commission Contract F14P-CT950011, Coordinated by the Dublin Institute for Advanced Studies, School of Cosmic Physics, Dublin, Ireland, Report 99–9–1 (1999).
43. Schraube, H., Mares, V., Roesler, S. and Heinrich, W. *Experimental Verification and Calculation of Aviation Routes Doses*. Radiat. Prot. Dosim. **86**(4), 309–315 (1999).
44. Armstrong, T. W., Chandler, K. C. and Barish, J. *Calculations of Neutron Flux Spectra Induced in the Earth's Atmosphere by Galactic Cosmic Rays*. J. Geophys. Res. **78**(16), 2715 (1973).
45. Ferrari, A., Pelliccioni, M. and Pillon, M. *Fluence to Effective Dose Conversion Coefficients for Neutrons up to 10 TeV*. Radiat. Prot. Dosim. **71**(3), 165–173 (1997).
46. Birattari, C., Rancati, T., Ferrari, A., Hofert, M., Otto, T. and Silari, M. *Recent Results at the CERN-EC High Energy Reference Field Facility*. In: Proc. Third Specialists Meeting on Shielding Aspects of Accelerators, Targets and Irradiation Facilities, Tohoku University, Sendai, Japan 12–13 May 1997, pp. 219–234.
47. Wilson, J. W. *Overview of Radiation Environments and Human Exposures*. In: Proc. 34th Annual Meeting of the National Council on Radiation Protection and Measurements, Washington, D.C., 1–2 April 1998 (available electronically from <http://techreports.larc.nasa.gov/ltrs/ltrs.html>).
48. Bartlett, D. T., Hager, L. G. and Tanner, R. J. *The Determination Using Passive Dosimeters of Aircraft Crew Dose: Results for 1997 ER-2 Flights*. In: Proc. The Atmospheric Ionizing Radiation (AIR) Investigators' Workshop, 30–31 March 1998, Langley, Virginia, NASA Report (1999) and private communication (1999).
49. Ferrari, A., Pelliccioni, M. and Rancati, T. *The Role of the Quantities Used in Radiological Protection for the Assessment of the Exposure to Cosmic Radiation*. Radiat. Prot. Dosim. **83**(3), 199–210 (1999).
50. Savitzky, A. and Golay, M. *Smoothing and Differentiation of Data by Simplified Least Squares Procedures*. Anal. Chem. **36**, 1627–1639 (1964).
51. *U.S. Standard Atmosphere, 1976* (Washington, DC: U.S. Government Printing Office) (1976).
52. Hendrick, L. D. and Edge, R. D. *Cosmic-Ray Neutrons Near the Earth*. Phys. Rev. **145**(4), 1023–1025 (1965).
53. Thomas, R. H. *Ionising Radiation Exposure Measurements at Commercial Jet Aircraft Altitudes*. Radiat. Prot. Dosim. **48**(1), 51–57 (1993).
54. Tennent, R. M. *Science Data Book* (Edinburgh: Oliver and Boyd) (1974).
55. Garcia-Munõz, M., Mason G. M. and Simpson, J. A. *The Anomalous ^4He Component in the Cosmic-Ray Spectrum at <50 MeV per Nucleon during 1972–1974*. Astrophys. J. **202**, 265–275 (1975).

56. Peters, B. *Cosmic Rays*. In: Handbook of Physics (New York: McGraw-Hill) pp. 9-201 to 9-244 (1958).
57. Gaisser, T. K. and Stanev, T. *Cosmic Rays*. Eur. Phys. J. **C3**, 132–137 (1998).
58. O'Brien, K. *Calculated Cosmic-Ray Ionization in the Lower Atmosphere*. J. Geophys. Res. **75**, 4357 (1970).
59. Brien, K. O. *The Theory of Cosmic-ray and High-energy Solar-particle Transport in the Atmosphere*, to be published.
60. Hajnal, F., McLaughlin, J., Weinstein, M. and O'Brien, K. *1970 Sea-level Cosmic-ray Neutron Measurements*. Report HASL-241 (New York: US Atomic Energy Commission) (1971).
61. Ferrari, A., Pelliccioni, M. and Pillon, M. *Fluence to Effective Dose Conversion Coefficients for Protons from 5 MeV to 10 TeV*. Radiat. Prot. Dosim. **71**(2), 85–91 (1997).
62. Ferrari, A., Pelliccioni, M. and Pillon, M. *Fluence to Effective Dose Conversion Coefficients for Muons*. Radiat. Prot. Dosim. **74**(4), 227–233 (1997).
63. Ferrari, A., Pelliccioni, M. and Pillon, M. *Fluence-to-effective Dose Conversion Coefficients for Negatively and Positively Charged Pions*. Radiat. Prot. Dosim. **80**(4), 361–370 (1998).
64. Ferrari, A., Pelliccioni, M. and Pillon, M. *Fluence to Effective Dose and Effective Dose Equivalent Conversion Coefficients for Photons from 50 keV to 10 GeV*. Radiat. Prot. Dosim. **67**(4), 245–251 (1996).
65. Ferrari, A., Pelliccioni, M. and Pillon, M. *Fluence to Effective Dose and Effective Dose Equivalent Conversion Coefficients for Electrons from 5 MeV to 10 GeV*. Radiat. Prot. Dosim. **62**(9), 97–104 (1997).
66. McCall, M. J. *Development and Validation of a Predictive Code for Aircrew Radiation Exposure (PC-AIRE)*. M. Eng. Thesis, Royal Military College of Canada (May 2000).
67. Dargahi, N. *The Ultimate Flight Simulator Pilot's Guidebook*. (New York: MIS Press) (1998).
68. O'Brien, K., Friedberg, W., Duke, F. E., Snyder, L., Darden, E. B. and Sauer, H. H. *The Response of Aircraft Crews to Radiation of Extraterrestrial Origin*. Radiat. Prot. Dosim. **45**, 145–162 (1992).
69. Bartlett, D. T., Hager, L. G., Irvine, D. and Bagshaw, M. *Measurements on Concorde of the Radiation Field at Aviation Altitudes*. Radiat. Prot. Dosim. **91**, 365–376 (2000).
70. Pelliccioni, M. (INFN, Laboratori Nazionali di Frascati. Private communication) (July 2000).
71. Noulty, R. (1996) (Bubble Technology Industries. Private communication.)
72. Tume, P., Lewis, B. J., Bennett, L. G. I. and Cousins, T. *Characterization of Neutron-sensitive Bubble Detectors for Application in the Measurement of Jet Aircrew Exposure to Natural Background Radiation*. Radiat. Nucl. Instrum. Methods Phys. Res. A **406**, 153–168 (1998).